NACA

RESEARCH MEMORANDUM

EFFECT OF WING HEIGHT AND DIHEDRAL ON THE LATERAL STABILITY

CHARACTERISTICS AT LOW LIFT OF A 45° SWEPT-WING AIRPLANE

CONFIGURATION AS OBTAINED FROM TIME-VECTOR ANALYSES

OF ROCKET-PROPELLED-MODEL FLIGHTS AT

MACH NUMBERS FROM 0.7 TO 1.3

By Clarence L. Gillis and Rowe Chapman, Jr.

Langley Aeronautical Laboratory
Langley Field, Va.

NATIONAL ADVISORY COMMITTEE
FOR AERONAUTICS
WASHINGTON
September 14, 1956

NATIONAL ADVISORY COMMITTEE FOR AERONAUTICS

RESEARCH MEMORANDUM

EFFECT OF WING HEIGHT AND DIHEDRAL ON THE LATERAL STABILITY

CHARACTERISTICS AT LOW LIFT OF A 45° SWEPT-WING AIRPLANE

CONFIGURATION AS OBTAINED FROM TIME-VECTOR ANALYSES

OF ROCKET-PROPELLED-MODEL FLIGHTS AT

MACH NUMBERS FROM 0.7 TO 1.3

By Clarence L. Gillis and Rowe Chapman, Jr.

SUMMARY

Lateral-stability flight tests were made over the Mach number range from 0.7 to 1.3 of models of three airplane configurations having 45° sweptback wings. One model had a high wing; one, a low wing; and one, a high wing with cathedral. The models were otherwise identical. The lateral oscillations of the models resulting from intermittent yawing disturbances were interpreted in terms of full-scale airplane flying qualities and were further analyzed by the time-vector method to obtain values of the lateral stability derivatives.

The effects of changes in wing height on the static sideslip derivatives were fairly constant in the speed range investigated and agreed well with estimated values based on subsonic wind-tunnel tests. Effects of geometric dihedral on the rolling moment due to sideslip agreed well with theoretical and other experimental results and with a theoretical relation involving the damping in roll. The damping in roll, when compared with theoretical and other experimental results, showed good agreement at supersonic speeds but was somewhat higher at a Mach number of 1.0 and at subsonic speeds. The damping in yaw showed no large changes in the transonic region.

The damping of the lateral oscillations for typical full-scale airplane flight conditions was marginal or unsatisfactory. In addition, the high-wing model had an undesirably high ratio of rolling motion to yawing motion.

INTRODUCTION

Attainment of flight speeds in the supersonic realm has focused attention on the stability problems associated with flight at high speeds and high altitudes. The types of lateral motions encountered and the importance of certain of the stability derivatives and inertia relations in defining the motions of the airplane have been examined. (See refs. 1 to 5, for example.) Techniques for determining the magnitude of the pertinent derivatives have been established for some time in the subsonic speed range. For supersonic speeds most of the tests have been made to determine the static lateral force and moment and the rolling moment due to sideslip and roll velocity. Recent work in the Langley 9-inch supersonic tunnel produced measurements of the rolling moment due to the rate of change of yaw and sideslip (ref. 6). Other techniques and measurements for the damping and cross derivatives are given in references 7 and 8. In order to furnish additional information on the lateral stability derivatives at transonic speeds, a rocket-propelled-model program to determine the effects of wing height and dihedral on the lateral stability characteristics of a $45°$ swept-wing airplane configuration has been conducted. The present paper reports the results obtained from three free-flight rocket-propelled models of this test program. The data were obtained on a high-wing model, a low-wing model, and a high-wing model with $10°$ cathedral.

An additional purpose of the present program was to provide further experience for evaluating the test technique and the time-vector method of data analysis. This method has been used previously for specific cases of both full-scale and model lateral-stability flight tests (refs. 9 to 12). The geometric variations utilized in the program to be discussed herein provided appreciable variations in frequency and very large variations in roll-to-yaw amplitude ratios. Some evaluation of the effects of these factors on the usefulness and accuracy of the test technique was possible.

The models were flight tested at the Langley Pilotless Aircraft Research Station at Wallops Island, Va.

SYMBOLS

C_C chord-force coefficient, $-a_l \dfrac{W}{qS}$

C_Y lateral-force coefficient, $a_t \dfrac{W}{qS}$

C_N normal-force coefficient, $a_n \dfrac{W}{qS}$

C_l rolling-moment coefficient, $\dfrac{\text{Rolling moment}}{qSb}$

C_n yawing-moment coefficient, $\dfrac{\text{Yawing moment}}{qSb}$

C_L lift coefficient, $C_N \cos \alpha - C_C \sin \alpha$

I_x moment of inertia about X-axis, slug-ft^2

I_z moment of inertia about Z-axis, slug-ft^2

I_{xz} product of inertia, $\dfrac{1}{2}(I_z - I_x) \tan 2\epsilon$, slug-ft^2

K_l span-load distribution factor, ft^2 (see appendix B)

L   concentrated load, lb (see appendix B)

M   Mach number

M_x, M_y, M_z rolling, pitching, and yawing moments about X, Y, and Z axes, respectively

P   period of lateral oscillation, sec

R   Reynolds number based on wing mean aerodynamic chord

S   wing area, sq ft

$T_{1/2}$ time required for lateral oscillation to damp to half amplitude, sec

V   velocity, ft/sec

W   weight of model, lb

X, Y, Z   coordinate axes

a   damping factor, $\dfrac{-0.693}{T_{1/2}}$, $\dfrac{1}{\text{sec}}$

a_l longitudinal accelerometer reading, positive in the positive x-direction, g units

a_n normal accelerometer reading, positive in the negative z-direction, g units

a_t lateral accelerometer reading, positive in the positive y-direction, g units

b wing span, ft

c local chord, ft

$\bar{c}$ mean aerodynamic chord, ft

$c_{1/2}$ number of cycles required for oscillation to damp to half amplitude

g gravitational acceleration, 32.2 ft/sec^2

k_x radius of gyration about X-axis, ft

k_z radius of gyration about Z-axis, ft

l rolling moment on a section of the wing, ft-lb (see appendix B)

l_a longitudinal distance between two transverse accelerometers, ft

m mass, slugs

p rolling velocity, radians/sec

q dynamic pressure, lb/sq ft, or pitching velocity, radians/sec

r yawing velocity, radians/sec

t time, sec

v_e equivalent lateral velocity, ft/sec

y spanwise station, ft

y' spanwise station at which concentrated load is applied, ft

α angle of attack, radians or deg

β angle of sideslip, radians or deg

Γ dihedral angle, deg, or span-load parameter (see appendix B)

ϵ principal-axis inclination, positive as shown in figure 5

$\eta = \dfrac{y}{b/2}$

θ pitch angle or angle of twist (see fig. 3 and appendix B), radians

μ_b relative mass density, $\dfrac{m}{\rho S b}$

ρ atmospheric density, slugs/cu ft

ϕ roll angle, radians

ψ yaw angle, radians

Ω_{C_Y} phase angle by which C_Y leads β

Ω_p phase angle by which p leads β

ω oscillation frequency, radians/sec

ω_n undamped natural frequency, radians/sec

Subscripts:

T   trim value

A   full-scale airplane

r   rigid

e   elastic

WF   wing-fuselage

V   vertical tail

W   wing

H   horizontal tail

A single dot over a symbol indicates the derivative of the quantity with respect to time; a double dot represents the second derivative with respect to time. Amplitude ratios of the oscillatory components of the motion are designated as $\left|\dfrac{C_Y}{\beta}\right|$, $\left|\dfrac{p}{\beta}\right|$, and so forth. The static stability

derivatives are indicated in the following manner: $C_{Y_\beta} = \dfrac{\partial C_Y}{\partial \beta}$, and so forth, whereas the rotary and acceleration derivatives are indicated as: $C_{n_r} = \dfrac{\partial C_n}{\partial \frac{rb}{2V}}$, $C_{n_{\dot\beta}} = \dfrac{\partial C_n}{\partial \frac{\dot\beta b}{2V}}$, and so forth.

MODELS AND INSTRUMENTATION

Models

Drawings and dimensions of the models are presented in figure 1. Additional geometric characteristics of the models are given in table I and the mass and inertia characteristics are given in table II. The three models had geometrically identical surfaces and fuselages and differed only in the vertical position and dihedral of the wing. The wing weight was counterbalanced so that the model center of gravity was on the geometric center line for all models.

Wings and tail surfaces had the quarter-chord line swept back 45° and had NACA 65A004 airfoil sections. The wings were composite wood and metal construction. Verical- and horizontal-tail surfaces were machined from solid duralumin. The horizontal-tail surface was set at an incidence angle of -1/2° with the fuselage center line for all models.

The fuselage was a parabolic body of revolution described by the coordinates given in table III. Housed in the spun-metal nose of the model was an electrically actuated yaw vane disturber. Photographs of the models are shown in figure 2.

In order to minimize the amount of pitch-yaw coupling encountered in the tests, the center of gravity of each model was placed very far forward (see table II) in an attempt to keep the pitch frequency always higher than twice the yaw frequency and thus avoid a resonant condition (ref. 13).

Throughout the remainder of this report, model 1 will designate the high-wing model, model 2, the low-wing model, and model 3, the high-wing model with cathedral.

Instrumentation

The models each contained an eight-channel NACA telemeter. The quantities recorded continuously were total pressure, angle of sideslip, rolling velocity, normal, longitudinal, and transverse accelerations near the center of gravity, transverse acceleration at the nose,

yaw-vane-disturber deflection (model 1 only), and angle of attack (models 2 and 3 only).

Ground-based instrumentation included a CW Doppler radar unit for measuring model velocity and acceleration, a modified SCR-584 radar unit for obtaining the model position in space as a function of time, and a rollsonde receiver operating on the telemeter-antenna radiation pattern as an additional measure of the model rolling velocity. Atmospheric conditions and wind velocities over the firing range were obtained from rawinsondes released immediately after the model flights. Manually operated 16-millimeter and 35-millimeter tracking cameras were used to photograph the model flight.

TESTS AND ANALYSIS

Preflight Tests

Because of the thin airfoil sections used, the model lifting surfaces were quite flexible. In order to obtain stiffness data, one wing panel and the vertical tail of one model were subjected to concentrated static loads at four points along both the 0.25 and 0.50 chord lines and the deflections along the leading and trailing edges measured. The results of the static loading tests are presented as influence coefficients in figure 3. The moments of inertia were determined by swinging the model as a pendulum and measuring the frequency of the oscillations. The principal longitudinal axis was determined by swinging the model in roll about a number of longitudinal axes inclined at various angles in the plane of symmetry and noting the angle for which the moment of inertia in roll was a minimum.

Flight Test

Each model was accelerated to a maximum Mach number of approximately 1.5 by a solid-fuel ABL Deacon rocket motor which separated from the model after burnout as a result of the relative drag-to-weight ratios. Figure 2(c) shows the high-wing model and booster on the launcher. The models contained no sustainer rockets. The yaw disturbers remained retracted during boosted flight and their operation was started at separation. The yaw vanes were programed to extend fully in a time of 0.33 second and retract in a time of approximately 0.05 second, the cycle being repeated every 1.4 seconds. Since the yaw vanes were set at a fixed angle of $10°$ with respect to the model center line, the model assumed a negative sideslip angle with the vanes extended. Upon the rapid retraction of the vanes, the model oscillated about the undisturbed trim conditions. The test conditions prevailing for the flights are presented in figure 4 as a function of the Mach number.

Corrections

Position corrections were required for some of the accelerometer readings to convert the measured values at the instrument location to values at the center of gravity. Corrections for model pitching and yawing velocities were also made to the readings of the air-flow indicators to obtain angles of attack and angles of sideslip. In the process of data analysis, all the measured lateral-oscillation data were referenced to β. The frequency-response characteristics of all the instruments were sufficiently close to those of the sideslip vane so that the only correction required was to the phase angle of the rolling velocity. This correction varied between approximately 1^O and 5° for the tests herein.

Analysis

The flight-test data presented herein were analyzed by the time-vector method of solution of the lateral stability equations of motion. The equations of motion used in the analysis and the assumptions involved are given in appendix A. References 9 to 12 contain detailed discussions of the method of solution. All the measured quantities used in the analysis and the resulting aerodynamic derivatives are referred to the system of body axes illustrated in figure 5.

Time histories of two typical oscillations for each of the three models are shown in figures 6, 7, and 8. For convenience in illustrating the important features of the motion, the mean values of rolling velocity have been subtracted from the data and only the disturbances superimposed on these mean values are shown in figures 6 to 8. The essentially steady-state or mean values of rolling velocity were caused by the slight amount of twist in the model wings. The most obvious differences between the motions for the three models are the greatly reduced oscillatory rolling velocities for models 2 and 3 compared with those of model 1. At speeds below about $M = 0.9$, model 3 exhibited no discernible periodic rolling motion. Also evident from figures 6, 7, and 8 is the lower frequency of the motion for model 1 compared with that of models 2 and 3.

In order to illustrate the effects of these motion characteristics on the analysis of the data herein, vector diagrams for $M \approx 1.2$ are shown in figure 9 for the high-wing model (model 1) and the low-wing model (model 2). The larger size of the side-force and yawing-moment diagrams for model 2 than for model 1 is a direct result of the higher frequency for model 2. The larger size of the rolling-moment diagram for model 1 is caused by its higher ratio of rolling to sideslipping motion. The side-force diagram shows that β and $-r$ are very nearly equal in magnitude and differ in phase angle by only a few degrees; these conditions justify the use of $\dot{\beta} = -r$ in the rolling-moment and yawing-moment equations.

For solution of the rolling-moment equation, it is necessary to know one of the aerodynamic derivatives before the other two can be found. For the high-wing model, $C_{l_r} - C_{l_{\dot\beta}}$ was estimated and then C_{l_p} and C_{l_β} were determined from the vector diagrams. It can be seen from figure 9(b) that $C_{l_r} - C_{l_{\dot\beta}}$ has a relatively minor effect on the motion of the high-wing model. When the same procedure was used for the low-wing model, very great scatter in the values of C_{l_p} occurred and some improbably high and some improbably low values resulted. It is evident in figure 9(b) that $C_{l_r} - C_{l_{\dot\beta}}$ has a much greater effect on the motion of the low-wing model. Comparisons of the two configurations (both at an angle of attack of nearly 0°) indicated that the contribution of the wing-body combination to C_{l_p} should be the same for the two models. Estimations of the contribution of the vertical tails to C_{l_p} (ref. 14) showed some differences for the two models because of the difference in sidewash produced by the rolling wings, but the entire contribution of the vertical tail was less than 5 percent of that due to the wing. Therefore, the values of C_{l_p} for the two configurations should be the same within a few percent. On the basis of this reasoning the values of C_{l_p} found for model 1 were assumed to apply for model 2 and the vector diagrams were completed to determine $C_{l_r} - C_{l_{\dot\beta}}$ and C_{l_β}.

In the yawing-moment diagrams (fig. 9(c)), it can be seen that the product of inertia and C_{n_p} terms have an appreciable effect on the motion for model 1, and a two-degree-of-freedom analysis of the yawing motion would be considerably in error. For model 2, however, neglecting the effects of the rolling motion would give a very good approximation to the yawing-moment derivatives. For solution of the yawing-moment equation, estimated values of $C_{n_p} = 0.02$ for model 1 and $C_{n_p} = 0.05$ for model 2 were used. These values were estimated by use of references 14 to 16 and the difference in value for the two models is due to the difference in sidewash at the vertical tail caused by the rolling wing. Reference 17, containing values of C_{n_p} for a swept-wing configuration at subsonic speeds, showed values of C_{n_p} no larger than 0.02 from $M = 0.4$ to $M = 0.95$.

For model 3 the analysis was similar to that for model 2 except that below a Mach number of about 0.95 where the rolling motion became essentially zero, all the rolling terms disappeared from the equations and it was not necessary to estimate any of the aerodynamic derivatives.

The measured values of C_Y were plotted against β and the slopes of these curves yielded the derivative C_{Y_β}. Since the phase angle

between C_Y and β was 180° for all models within the accuracy to which this quantity could be measured, the amplitude ratio $\left[\dfrac{C_Y}{\beta}\right]$ is equal to $-C_{Y_\beta}$.

The flexibility of the wings and vertical-tail surfaces of the models had an appreciable effect upon the results. The effects of wing flexibility on C_{l_p} and the increment in C_{l_β} caused by geometric dihedral and the effects of vertical tail flexibility on C_{Y_β}, C_{n_β}, and C_{n_r} were estimated by the methods outlined in appendix B.

Accuracy

An investigation of the accuracy of the lateral stability derivatives was made as in reference 9. Two Mach numbers (1.3 and 0.7) were selected and the investigation was made for models 1 and 2. The results for model 2 should also apply approximately to model 3.

From previous experience with similar instrumentation and by inspection of the data described herein, the accuracies of the basic measured quantities were estimated and are shown in table IV. The increments in the various derivatives caused by errors of these magnitudes were then determined mostly graphically from the vector diagrams. The resulting increments are shown in table V. The probable errors in table V are given in terms of both absolute magnitude and as percentages of the derivatives. The percentage errors have little meaning in some cases, such as for C_{l_β} of model 2 for example, where the absolute error is small but the percentage error is large because C_{l_β} is near zero. Also shown in the lower parts of table V are the increments caused by certain amounts of uncertainty in the aerodynamic derivatives that had to be estimated to permit determination of the other derivatives.

From table V it is evident that the static sideslip derivatives are, in general, more accurately determined than are the rotary derivatives. When the effect of dynamic pressure inaccuracies which have an appreciable effect on all derivatives at low speeds is excluded, the values of C_{n_β} are affected greatly by inaccuracies in P; the values of $C_{n_r} - C_{n_\beta^\cdot}$, by inaccuracies in $T_{1/2}$; the values of C_{l_β}, by inaccuracies in $\left|\dfrac{p}{\beta}\right|$; and the values of $C_{l_r} - C_{l_\beta^\cdot}$, by inaccuracies in Ω_p. When the rolling velocity is large, additional large effects on C_{n_β} and $C_{n_r} - C_{n_\beta^\cdot}$ are caused by inaccuracies in ϵ and α, and C_{l_p} and C_{l_β} are also affected greatly by inaccuracies in Ω_p. An understanding of the reasons for all these effects can be obtained by a study of the vector diagrams in figure 9.

The effect of uncertainties in the estimated value of C_{n_p} is fairly large for the yaw damping $C_{n_r} - C_{n_{\dot{\beta}}}$ for model 1 and fairly small for model 2, even though the estimated value is larger for model 2. This effect, of course, is again due to the great difference in the amplitude of the rolling motion between the two models. Errors in the values of C_{l_p} and $C_{l_r} - C_{l_{\dot{\beta}}}$ used in the analysis have appreciable effects on each other. However, because of the method of obtaining these derivatives for the present series of tests, as explained in the Analysis section, these quantities should be subject to less uncertainty than are the values of C_{n_p}.

RESULTS AND DISCUSSION

Time Histories

Portions of the model time histories were presented previously in figures 6 to 8 and some characteristics of the lateral motions were pointed out. Small variations, mostly of a random character, occurred in the angle-of-attack and lift-coefficient time histories; these variations raise the question of inertia coupling between longitudinal and lateral motions. Although the effects of the lateral motion on the longitudinal motion were important in producing or modifying the longitudinal motion shown in figures 6 to 8, the factor of significance for the data presented herein is the secondary effect of this longitudinal motion on the lateral motion. Calculations indicated that these latter effects were within the accuracy of the measurements for the data presented herein.

Trim Characteristics

The trim values or mean values of the measured quantities with oscillatory components removed are shown in figure 10. These mean values are a measure of the asymmetry of the models or the measuring instruments. In particular, the positive value of C_{Y_T} for model 1 is believed to represent a constant-acceleration error (or zero shift) in the transverse accelerometer at the center of gravity. This supposition is supported by the nonzero mean values which occurred in the values of $\dot{\psi}$ for this model, as calculated from the difference in readings between the accelerometers at the center of gravity and in the nose. Both of these discrepancies are of a magnitude and direction to be explained by the acceleration error mentioned.

All models remained near zero lift. The mean values of rolling velocity are given in terms of the helix angle $pb/2V$, which was less than 0.01 for all models. The estimated α for model 1 shows the values used in the solution of the equations and was obtained by dividing the measured C_{N_T} by an estimated C_{N_α}, since α was not measured on this model.

Oscillation Characteristics

The measured periods of oscillation are shown in figure 11. The most obvious feature is the larger periods for the high-wing model. The damping characteristics are shown in figure 12. Little difference in magnitude existed between the damping times for the three models.

The amplitude ratios of rolling velocity to sideslip angle are shown in figure 13. The ratio for the high-wing model is 5 to 10 times as high as for the other two models. For both high-wing models, the rolling-velocity amplitude ratio increases considerably as the Mach number increases, whereas for the low-wing model it is more nearly constant. The 10° cathedral in the high-wing caused roughly the same decrease in rolling velocity as moving the wing to the low position.

The phase angle by which the rolling velocity leads the sideslip angle is shown in figure 14. Below $M = 0.90$, no values could be determined for model 3 because of the lack of any measurable oscillatory rolling velocity. Model 2 exhibits considerably larger variations of phase angle with Mach number than does model 1. At least part of this variation can be attributed to a lesser degree of experimental accuracy in determining the phase angles for model 2 because of the smaller amplitudes of rolling motion. This is indicated in table IV by the smaller accuracy listed for model 2.

Plots of C_Y against β are shown in figure 15. Within the random scatter of the data the curves appear to be linear for models 1 and 2. For model 3 some possible nonlinearity is evident in the Mach number region from 0.74 to 0.83, although linear slopes are faired through the data points in figure 15(c) for purposes of data analysis. The more acute angle at the wing-fuselage juncture for this model may be a source of flow separation leading to possible nonlinearities. No fairings of the wing-fuselage juncture were used on any of the models. As indicated by the vector diagrams in figure 9, the effects of change in slope of the curve of C_Y plotted against β will be very small. The main significance of any nonlinearities in the curve of C_Y against β is that this result indicates the possibility of nonlinearities in other derivatives. Because the analysis used herein is a linear analysis, the derivatives obtained represent averages over the sideslip range of the tests.

From the previous plots, slopes of the side-force coefficient as a function of sideslip angle have been determined and the derivative C_{Y_β} as a function of Mach number is presented in figure 16. The high-wing model, as would be expected, has a lower C_{Y_β} than does either of the other models. In the transonic region the low-wing model has a value of C_{Y_β} 25 to 50 percent greater than the high-wing model. The values

of C_{Y_β} for the high-wing model with cathedral fall between those for
the other two models, these values being generally closer to those for
the low-wing model. In the region of possible nonlinearity, the
slopes C_{Y_β} for model 3 exhibit some rather large and irregular vari-
ations with Mach number. As indicated in figure 16, vertical-tail
flexibility had a relatively small effect on C_{Y_β}.

The preceding plots present the basic information which, with the
mass and inertia characteristics given in tables I and II, constitute
the data necessary to construct the vector diagrams. Quantities from
the plots of period, amplitude ratio, and phase angle were not faired
before using them to construct the vector diagrams since each point in
effect constitutes a faired value to the extent that periods, amplitude
ratios, and phase angles are for a number of half cycles of the oscil-
lations. A faired value was used for $T_{1/2}$ in the data reduction because
of the difficulty in obtaining an accurate value of this quantity.

Figure 17 shows a comparison of the amplitude ratio of yawing accel-
eration to sideslip angle for two models as measured from the transverse
accelerometers by the relation

$$\dot{r} = \frac{\left(a_{t_{nose}} - a_{t_{cg}}\right)g}{l_a}$$

and as determined from the vector-diagram solutions. The agreement shown
is considered to be very good and furnishes a check on the accuracy of
the solutions. The comparison in figure 17 also is a further indication
of the small magnitude of coupling effects because the difference in
reading between two transverse accelerometers separated along the X-axis
will actually be proportional to the sum $(\dot{r} + pq)$.

Lateral Stability Derivatives

The sideslip derivatives are presented for β in degrees to facil-
itate comparisons with wind-tunnel test results. In the equation of motion
these derivatives must be used with β in radians. The static stability
derivative C_{n_β} is presented as a function of Mach number in figure 18.
In agreement with the high value of sidewash expected for a high-wing
configuration (ref. 18), the static stability derivative of the high-wing
model is consistently lower than that for either of the other two models.
An approximately constant difference exists between the high- and low-
wing models. The static stability derivative of model 3 is slightly lower
than that for the low-wing configuration at subsonic Mach numbers but is
approximately the same at supersonic Mach numbers. Hence, it appears that
the lower values for C_{Y_β} for model 3 than for model 2 (fig. 16) at super-
sonic speeds may not be a result of sidewash effects on the vertical tail

but may be a wing-fuselage effect. The effect of vertical-tail flexi-
bility is greater for the low wing than for the high-wing model because
at a given sideslip angle the vertical-tail load is greater for the low-
wing model as a result of the smaller sidewash.

The variation of the effective dihedral derivative C_{l_β} with Mach
number is presented in figure 19. The high-wing model had a large neg-
ative value of C_{l_β} which rose to a peak at $M = 1.0$ and decreased in
magnitude at supersonic speeds. The values of C_{l_β} for the low-wing
model were approximately one-fourth as large as those for the high-wing
model. The variation of the derivative with Mach number for the model
with cathedral was such that the values of C_{l_β} were lower than that for
the low-wing model at subsonic speeds but increased greatly at Mach
numbers above 1.0 and became greater than that for the low-wing model at
the highest speeds attained in the tests.

An exact estimate of the effects of flexibility on C_{l_β} would be very
involved since both wing and vertical tail contribute to C_{l_β}, and the
wing load distribution and resulting sidewash changes as affected by wing
height are unknown. The increment in C_{l_β} contributed by the vertical
tail will be reduced by vertical-tail flexibility but this reduction will
be small (about 9 percent at the highest Mach number) and will be nearly
the same for all three models. The increment in C_{l_β} caused by moving
the wing to the top or bottom of the fuselage is essentially a wing-root
effect and the influence coefficients in figure 3 indicate very little
wing twist due to loads concentrated near the inboard end. Therefore, to
a first approximation, the values of C_{l_β} for the high- and low-wing
models should be relatively unaffected by wing and tail flexibility. The
increment in C_{l_β} caused by the geometric dihedral is shown by refer-
ence 19 and data to be presented subsequently herein to be approximately
proportional to C_{l_p}, although, of course, the load distributions are not
identical. Therefore, as a gross approximation, the increments in C_{l_β}
due to geometric dihedral were corrected by the same factor calculated
for C_{l_p} and the results are shown in figure 19.

As discussed in the Analysis section, the damping-in-roll deriv-
ative C_{l_p} was determined for model 1 only and it was assumed that
the C_{l_p} for models 2 and 3 was the same. Accordingly, the variation
of C_{l_p} with Mach number for the models is shown in figure 20. The
effect of wing flexibility on C_{l_p} was very large, the estimated incre-
ment due to elasticity being about 50 percent of the measured value
at $M = 1.3$. The C_{l_p} data are almost entirely a wing-fuselage effect

since, as mentioned previously, the tail surfaces contribute less than
5 percent of the damping in roll when the effect of the rolling wake on
the tail is accounted for.

Presented in figure 21 is the variation of the damping-in-yaw deriv-
ative $C_{n_r} - C_{n_{\dot{\beta}}}$ with Mach number. As might be accounted for by
the high rate of change of sidewash, the damping-in-yaw derivative for
the high-wing model is generally higher than the damping for either of
the other two models, although the differences approach the order of
accuracy (table V). Both models 2 and 3 show irregular variations in
the supersonic region. No large loss in damping occurred near a Mach
number of 1.0 as has generally been experienced for the pitch damping
of sweptback configurations (ref. 20). Flexibility of the vertical
tail caused an estimated loss in yaw damping of about 9 percent at the
highest Mach number. Since this value is less than the calculated
probable accuracy of the derivatives, it is not shown in figure 21.

The variation of the cross derivative $C_{l_r} - C_{l_{\dot{\beta}}}$ with Mach
number is shown in figure 22. The solution for the model with cathedral
at subsonic speed is relatively independent of the assumption for C_{l_p}
since the excitation of the roll approached zero below $M = 1.0$.
Above $M = 1.0$, the $C_{l_r} - C_{l_{\dot{\beta}}}$ for this model rises rapidly. For the
low-wing model, the cross derivative has an erratic variation through
the transonic region with a slightly negative value in the region
around $M = 0.85$. Because of the relatively large possible inaccuracies
in this derivative (table V) and the unknown aerodynamic interference
effects, no attempt was made to estimate the effects of flexibility.

Comparison With Other Data

Figures 23 to 25 contain summary plots comparing the data described
herein to various wind-tunnel, rocket-propelled model, and theoretical
results on similar configurations. The rocket-propelled model data of
reference 21 are for wing and tail geometry identical to the models of
the present tests except for a midwing position. The fuselage shape was
somewhat different. The wind-tunnel data at Mach numbers of 2.01
(ref. 22) and 1.41 (unpublished) were for the same wing as the present
tests but a different empennage arrangement. (See fig. 23.) The wind-
tunnel data at $M = 0.17$ (ref. 18) and $M = 0.80$ to 0.92 (ref. 23)
were for configurations with somewhat different wing and tail geometry.
All these wind-tunnel data have been corrected for the differences in
tail geometry for comparison with the present tests.

The curves shown in figures 23 to 25 for the present tests are those
labeled "estimated rigid" in previous figures since the wind-tunnel data

are for essentially rigid models. In addition, the values of C_{n_β} for the present tests have been adjusted to a center-of-gravity position at $0.20\bar{c}$ to furnish a more valid comparison with data in reference 21 (center of gravity at $0.19\bar{c}$) and references 18 and 22 (center of gravity at $0.25\bar{c}$).

Results for the midwing rocket-propelled model of reference 21 agree very well with the sideslip derivatives of the present test (fig. 23) except for C_{n_β} at $M = 1.3$ where the values from reference 21 are somewhat higher than would be expected for a midwing configuration from the present tests. The increment in C_{Y_β} and C_{n_β} caused by changes in wing height, at an angle of attack of 0°, are caused by the vertical tail being in different regions of the sidewash field for the different wing positions. These increments for the present test are about the same as those obtained from the subsonic wind-tunnel data of reference 18 where a somewhat similar vertical tail was used and are somewhat larger than the increments from reference 23. The supersonic wind-tunnel data at $M = 1.41$ and $M = 2.01$ show much smaller increments resulting from changes in wing height. This condition is caused by the smaller changes in sidewash on the vertical tail for these tests as a result of the vertical tail being effectively nearer the center of the sidewash field. A vertical tail having its area symmetrically distributed above and below the longitudinal body axis would produce no change in C_{Y_β} and C_{n_β} at an angle of attack of 0° as the wing is moved from the bottom to the top of the fuselage.

The increments in C_{l_β} caused by changes in wing height are primarily an effect of the wing and secondarily, an effect of the tail. These increments are reasonably constant throughout the Mach number range from 0 to 2.0, some increase occurring at transonic speeds. The comparison between the various sets of data for C_{l_β} in figure 23 is very good. No theoretical values are shown in figure 23 because no theoretical values of sidewash resulting from the load distributions due to wing-height changes are available.

A summary of the effects of geometric dihedral on C_{l_β} is shown in figure 24. The approximate method of reference 19 when used with the experimental (flexible) values of C_{l_p} from the present test showed remarkable agreement with the experimental values. This fact formed the basis for the method of correcting the C_{l_β} value of the high wing with cathedral model for flexibility as described previously. The subsonic theory of reference 24 and the supersonic wind-tunnel data of reference 25 show values of $\dfrac{C_{l_\beta}}{\Gamma}$ similar to those for the present tests.

The values of C_{l_p} from the present test corrected to rigid-wing values (fig. 25) are somewhat higher at subsonic speeds than those attained from wind-tunnel data (ref. 17) or theoretical values (ref. 24), are considerably higher than the theory of reference 26 at $M = 1.0$, and are in very good agreement with the theoretical values in reference 27 at supersonic speeds. The unpublished rocket-propelled-model data in figure 25 are for a midwing model with a wing having the same aspect ratio and sweepback as the wing of the present tests but less taper and thicker airfoil. These data show good agreement with the present tests at supersonic speeds but show a lower peak at $M = 1.0$. The curve for the present test, when extrapolated, would indicate a slightly higher C_{l_p} than the data in reference 21 which were for the same wing and tail arrangement. This is reasonable since the data of reference 21 were not corrected for flexibility.

Little information exists on the derivative $C_{l_r} - C_{l_{\dot\beta}}$ for comparison with the present tests. Calculated values from reference 15 at low subsonic speeds were about 0.04 which is at least the correct order of magnitude. (See fig. 22.) Reference 6 contains measurements of $C_{l_r} - C_{l_{\dot\beta}}$ at supersonic speeds for a swept-wing configuration, and the values obtained were much larger than those estimated, the reason for this not being obvious from the tests.

Flying Qualities

The motion characteristics presented previously for the three models may be interpreted in terms of full-scale airplane flying qualities. The nondimensional characteristics of the motion, that is, amplitude ratios such as $\left|\dfrac{\phi}{\beta}\right|$, phase angles, and number of cycles required to damp to a given fraction of the original amplitude may be considered as applying directly to a full-scale airplane having the same relative density and the same nondimensional radii of gyration.

The relative density factor μ_b for the model tests varied from about 115 at a Mach number of 0.7 to about 87 at a Mach number of 1.3. The full-scale airplane altitudes and wing loadings represented by these values, the models flown being assumed to be 1/10-scale models, are shown in figure 26. The values simulated by the models are reasonable for current aircraft.

Requirements for damping of the lateral oscillations for military aircraft are given in reference 28. These requirements are illustrated in figure 27. Points for all three models discussed herein are shown on the chart for two Mach numbers. It is apparent that the damping is marginal or unsatisfactory for all three configurations for normal-flight

conditions and would require augmentation to satisfy tactical-mission requirements (gunnery or bombing runs).

A comparison was made of the nondimensional radii of gyration of the three models with average values for three current swept-wing fighter aircraft. The comparison showed that the radii of gyration in roll were the same but that the radii of gyration in yaw of the models were about 15 percent larger than those for the full-scale airplanes. Also, as stated previously, the centers of gravity of the models were placed near the leading edge of the mean aerodynamic chords to minimize pitch-yaw coupling. A normal center-of-gravity position for this type of aircraft would probably be near 30 percent of the mean aerodynamic chord. The effects on the motion of reducing the radius of gyration in yaw by 15 percent and the effects of this reduction combined with a 30-percent rearward movement of the center of gravity were investigated for the high-wing model at a Mach number of 1.3. This point was chosen since it represents the lowest static stability measured during the present tests and thus would be expected to produce the largest effects. The stability derivative C_{n_β} and the damping derivative $C_{n_r} - C_{n_{\dot{\beta}}}$ were transferred to the altered center-of-gravity position. Since the transfer equations for C_{n_r} and $C_{n_{\dot{\beta}}}$ are different, this procedure cannot be done rigorously since only the quantity $C_{n_r} - C_{n_{\dot{\beta}}}$ is known. Wind-tunnel tests and estimated results, however, indicate that $C_{n_{\dot{\beta}}}$ should be small compared with C_{n_r} at low lift and that C_{n_r} is nearly all caused by the vertical tail. Therefore, the damping derivative $C_{n_r} - C_{n_{\dot{\beta}}}$ was reduced by the square of the ratio of vertical-tail distances from the two center-of-gravity positions. Solutions for these altered conditions were made with the aerodynamic derivatives as known quantities to obtain the motion characteristics. The results are shown in figure 27. Reducing the radius of gyration caused the motion to move further into the satisfactory region. When this condition was combined with a rearward center-of-gravity movement, the motion became definitely unsatisfactory. This latter result is contrary to what might be expected if a simple yawing oscillation is considered. The calculations showed that it was caused by the product-of-inertia effect assuming relatively greater importance when the aerodynamic derivatives C_{n_β} and $C_{n_r} - C_{n_{\dot{\beta}}}$ were reduced by the rearward center-of-gravity movement.

An additional desirable quality for the lateral oscillatory motion is that the ratio $\left|\frac{\phi}{\beta}\right|$ should not exceed about 4 (ref. 29) to preclude excessive rolling motions resulting from small corrections in heading or from flight through rough air. Figure 28 shows the values of $\left|\frac{\phi}{\beta}\right|$ for the three models. For the high-wing model, the ratio $\left|\frac{\phi}{\beta}\right|$ remains

above 5 for all Mach numbers. For the other two models, $\left|\dfrac{\phi}{\beta}\right|$ remains below 2 over the Mach number range investigated.

CONCLUSIONS

Lateral stability investigations were made at low angles of attack by flight tests between Mach numbers of about 0.7 and 1.3 of three rocket-propelled models of a swept-wing airplane configuration, one having a high wing, one a low wing, and one a high wing with 10° cathedral. Analysis of the motions following yawing disturbances and comparisons with other investigations indicated the following conclusions:

1. Increments in the static lateral stability derivatives caused by moving the wing from a high to a low position were roughly constant in the transonic region and were of the same magnitude as the increments estimated for these configurations based on low-speed wind-tunnel data for a similar configuration.

2. Estimates based on supersonic wind-tunnel data showed smaller increments due to wing-height changes on the static lateral-force and yawing-moment derivatives than the present tests. This difference can be explained by the differences in vertical-tail geometry resulting in different magnitudes of sidewash effect.

3. The change in the static rolling-moment derivative due to wing height, which is primarily a wing-fuselage effect, was of a similar magnitude for the present tests and the supersonic wind-tunnel tests which used the same wing and a similar fuselage.

4. The effect of geometric dihedral on the static rolling-moment derivative showed good agreement with subsonic theoretical results and with a theoretical relationship between this derivative and the experimental damping in roll.

5. The damping in roll, when corrected to rigid-wing values and compared with theoretical and other experimental data (on midwing configurations) showed very good agreement at supersonic speeds but was somewhat high at subsonic and transonic speeds.

6. When interpreted in terms of full-scale airplane flying qualities, the damping of the lateral oscillations of these configurations was not sufficient and augmented damping would be required. In addition, the

ratio of rolling motion to sideslipping motion for the high-wing config-
uration was undesirably large.

Langley Aeronautical Laboratory,
      National Advisory Committee for Aeronautics,
            Langley Field, Va., May 4, 1956.

APPENDIX A

EQUATIONS OF MOTION

All the measured quantities used in the lateral-stability analysis herein and the resulting aerodynamic derivatives are referred to the system of body axes illustrated in figure 5. The three equations of motion used to represent the free-oscillation response of the models in the lateral mode following a disturbance were:

$$\frac{mV}{qS}(\dot{\beta} + r - \alpha p) - C_Y = 0 \tag{A1}$$

$$\frac{I_x}{qSb}\dot{p} - \frac{I_{xz}}{qSb}\dot{r} - C_{l_\beta}\beta - C_{l_p}\frac{pb}{2V} - \left(C_{l_r} - C_{l_{\dot{\beta}}}\right)\frac{rb}{2V} = 0 \tag{A2}$$

$$\frac{I_z}{qSb}\dot{r} - \frac{I_{xz}}{qSb}\dot{p} - C_{n_\beta}\beta - C_{n_p}\frac{pb}{2V} - \left(C_{n_r} - C_{n_{\dot{\beta}}}\right)\frac{rb}{2V} = 0 \tag{A3}$$

In the side-force equation (A1) the gravity terms $\frac{W}{qS}(\phi \cos \theta + \psi \sin \theta)$ have been omitted. As shown in the Accuracy section of this report, this omission has a negligible effect on the results presented herein and eliminates the necessity of measuring or computing the roll, pitch, and yaw angles. Also in equation (A1) the total aerodynamic side force is given by C_Y and includes the contributions of C_{Y_β}, $C_{Y_{\dot{\beta}}}$, C_{Y_p}, and C_{Y_r} because this is the quantity obtained from the transverse accelerometer by the relation $C_Y = a_t \frac{W}{qS}$.

In equations (A2) and (A3), the assumption has been made that $\dot{\beta} = -r$ in order that the yawing- and sideslipping-velocity derivatives may be combined to reduce the number of unknown aerodynamic terms. As shown by the vector diagrams in figure 9, this is a very good approximation for the tests discussed herein.

Detailed discussions of the application of the time-vector method to the solution of equations (A1) to (A3) may be found in references 9 to 12.

The vector solution of the equations of motion is illustrated in figure 9. All quantities are referenced to β having an amplitude scale shown on the diagrams and zero phase angle. Only two of the three derivatives in each of the rolling-moment and yawing-moment equations can be determined from one set of test conditions by the method of solution described herein. The methods of approximation used in the solution are

discussed in the Analysis section of this report and some comments on extension of the test technique to include other modes of motion and other test conditions are included in appendix C.

For model 3 the oscillatory rolling velocity was zero at subsonic speeds and for this case equations (A1) to (A3) simplify to

$$\frac{mV}{qS}\,(\dot{\beta} + r) - C_Y = 0 \qquad\qquad (A4)$$

$$\frac{-I_{xz}}{qSb}\,\dot{r} - C_{l_\beta}\,\beta - \left(C_{l_r} - C_{l_{\dot{\beta}}}\right)\frac{rb}{2V} = 0 \qquad\qquad (A5)$$

$$\frac{I_z}{qSb}\,\dot{r} - C_{n_\beta}\,\beta - \left(C_{n_r} - C_{n_{\dot{\beta}}}\right)\frac{rb}{2V} = 0 \qquad\qquad (A6)$$

Since C_{l_p} and C_{n_p} are eliminated from the equations, it was not necessary to estimate any of the derivatives for solution of equations (A4) to (A6).

APPENDIX B

EFFECTS OF FLEXIBILITY OF VERTICAL TAIL AND WING

Vertical Tail

The effect of vertical-tail flexibility on the vertical-tail lift-curve slope was calculated by the method of reference 30. For this calculation the influence coefficients in figure 3 and the span-load distributions of reference 31 were used. The loss in vertical-tail lift-curve slope due to flexibility was 9 percent at a Mach number of 1.3 and 1 percent at a Mach number of 0.7. Estimated rigid values for the derivatives C_{Y_β} and C_{n_β} were then obtained from

$$C_{Y_{\beta,r}} = \left(C_{Y_{\beta,e}} - C_{Y_{\beta,WF}}\right) \frac{C_{L_\alpha,Vr}}{C_{L_\alpha,Ve}} + C_{Y_{\beta,WF}}$$

and

$$C_{n_{\beta,r}} = \left(C_{n_{\beta,e}} - C_{n_{\beta,WF}}\right) \frac{C_{L_\alpha,Vr}}{C_{L_\alpha,Ve}} + C_{n_{\beta,WF}}$$

The values of C_{Y_β} and C_{n_β} for the wing-fuselage combination were estimated from wind-tunnel tests.

Wing

The effect of wing flexibility on C_{l_p} was calculated by the method of reference 30 with some modifications to obtain rolling-moment effects rather than lift effects. The influence coefficients used are shown in figure 3 and the span-load distribution was obtained from reference 24.

The equations herein represent the right wing of the airplane with a positive load L producing negative rolling moment. The wing and span-load distribution are divided into a number of sections as in reference 30. The C_{l_p} for the elastic wing is given by

$$C_{l_{p,e}} = \frac{2(l_1 + l_2 + \cdots)}{qSb \, \dfrac{pb}{2V}} \tag{B1}$$

The rolling moment produced by section 1 of the elastic wing can be approximated by

$$l_1 = C_{l_{p,r}}\left(\frac{pb}{2V} + \frac{\Delta\alpha_1}{\eta_1}\right)\frac{qSb}{2}K_1\frac{b}{2}\eta_1^2 \qquad (B2)$$

where

$$K_1 = S\frac{\displaystyle\int_{\eta_{1_i}}^{\eta_{1_o}}\Gamma(p)\frac{d\eta}{\eta}}{\displaystyle\int_{\eta_o}^{1.0}\Gamma(p)\eta\,d\eta}$$

$\Gamma(p)$　　　　　span-load parameter for rolling wing

$\Delta\alpha_1$　　　　　change in section angle of attack caused by wing elasticity

η_1　　　　　value of η at centroid of load distribution over section 1

η_o　　　　　value of η at root of exposed wing

η_{1_i}　　　　　value of η at inboard end of section 1

η_{1_o}　　　　　value of η at outboard end of section 1

From equation (B2)

$$\frac{\Delta\alpha_1}{pb/2V} = \frac{l_1\eta_1}{K_1\frac{b}{2}\eta_1^2 C_{l_{p,r}}q\frac{pb}{2V}} - \eta_1 \qquad (B3)$$

or since

$$l_1 = -L_1\eta_1\frac{b}{2} \qquad (B4)$$

$$\frac{\Delta\alpha_1}{pb/2V} = \frac{-L_1}{K_1C_{l_{p,r}}q\frac{pb}{2V}} - \eta_1 \qquad (B5)$$

From the influence coefficients the change in angle of attack at section 1 may be obtained as

$$\frac{\Delta\alpha_1}{pb/2V} = \frac{L_1}{pb/2V}\theta_{11} + \frac{L_2}{pb/2V}\theta_{12} + \cdots \quad (B6)$$

where θ_{ij} is the twist at station i due to a unit load at station j. Equating (B5) and (B6) and rearranging yields

$$\frac{L_1}{pb/2V}\left(\theta_{11} + \frac{1}{K_1 C_{l_{p,r}}q}\right) + \frac{L_2}{pb/2V}\theta_{22} + \cdots = -\eta_1 \quad (B7)$$

Similar equations are written for each section and the resulting set of equations is solved simultaneously for the values of $\dfrac{L_1}{pb/2V}$, $\dfrac{L_2}{pb/2V}$, and so forth, for various values of $C_{l_{p,r}}q$ covering the test range. Then from equations (B1) and (B4) and the values of $\dfrac{L_1}{pb/2V}$, $\dfrac{L_2}{pb/2V}$, and so forth, the ratio of elastic damping in roll to rigid damping in roll is given by

$$\frac{C_{l_{p,e}}}{C_{l_{p,r}}} = -\frac{\left(\dfrac{L_1}{pb/2V}\eta_1 + \dfrac{L_2}{pb/2V}\eta_2 + \cdots\right)}{C_{l_{p,r}}qS} \quad (B8)$$

In addition to its use in correcting C_{l_p} for wing flexibility, equation (B8) was used to give a first approximation to the effects of wing flexibility on the increment of C_{l_β} caused by geometric dihedral, as explained in the text.

APPENDIX C

EVALUATION OF TEST TECHNIQUE

Analysis of the data for the three configurations discussed herein provided some comparative basis for evaluating the test technique. The most obvious conclusion is that no general statements applicable to all cases can be made and each case must be examined individually to determine the aerodynamic derivatives that can be determined and their resultant accuracy.

The primary weakness in the test technique is that not all the rolling-moment and yawing-moment derivatives usually included in the equations of motion can be determined. This is a result of the fact that the Dutch roll lateral oscillation when analyzed by the time-vector method does not by itself furnish sufficient information for determining all the derivatives. Some approximations must be made to permit the determination of the most important derivatives. One approximation generally made is that $\dot{\beta} = -r$ which reduces the number of unknown derivatives by 2.

In many cases the cross derivatives C_{n_p} and $C_{l_r} - C_{l_{\dot{\beta}}}$ have relatively small effects on the motion and their magnitude may safely be estimated to permit determination of the other derivatives. For some cases where the effects of C_{n_p} or $C_{l_r} - C_{l_{\dot{\beta}}}$ may be appreciable but not necessarily larger than the effects of other derivatives, it may be advantageous to use estimated values of some of the other derivatives such as C_{l_β}, C_{l_p}, or $C_{n_r} - C_{n_{\dot{\beta}}}$ because of the relatively greater amount of information available on these derivatives.

It is also fairly obvious that the rolling derivatives C_{l_p} and C_{l_β} are best obtained from motions involving a large ratio of rolling to yawing motion and the yawing derivatives C_{n_β} and $C_{n_r} - C_{n_{\dot{\beta}}}$ are best obtained from motions having a large ratio of yawing motions to rolling motion, because these conditions tend to minimize the effects of the cross derivatives. Conversely, the effects of the cross derivatives can be increased by reversing these conditions. Thus, intelligent planning of the dynamic conditions of the tests can result in emphasizing the derivatives of most interest.

Alterations in the ratio of rolling motion to yawing motion may be accomplished by changing the ratio of rolling moments of inertia to yawing moments of inertia. If two flights at two different inertia ratios but

under otherwise identical conditions can be made, then the difficulty of having too many derivatives to measure can be obviated, because two different sets of motions would be available. Both sets of motions must be produced by the same set of derivatives, and thus a larger number of derivatives may be determined.

In order to assist in analyzing the data other modes of motion may be used, such as the heavily damped roll subsidence. The damping of this motion is almost completely dependent upon C_{l_p}, the other derivatives having only a negligible effect, and may be used to find C_{l_p} if this mode of motion can be extracted from the measured time histories. This procedure has been used in other unpublished rocket-propelled model tests to measure C_{l_p}. For the present tests the time to damp to half amplitude of this mode of motion was about 0.03 second at $M = 1.3$ and 0.06 second at $M = 0.7$ and examination of the time histories indicated that this motion could not be extracted from the results. Greater excitation of this mode of motion can be obtained by applying a rolling-moment disturbance rather than a yawing-moment disturbance as for the present tests.

Although the test technique used is a dynamic technique, the analysis of these and other flight test data indicated that the so-called static sideslip derivatives can usually be determined more accurately than can the rotary derivatives. The rotary derivatives depend primarily on the phase relations between the various components of motion and a more accurate determination of the rotary derivatives would require greater accuracy in the measurement of the phase angles and of those quantities which effectively cause phase shifts in the motion, such as angle of attack, inclination of the principal axis, and the damping of the motion. The requirement for accuracy of measurement of the phase angles also requires that the frequency-response characteristics of each instrument be known, since appreciable errors in phase angles due to imperfect instrument response may be present in the data and must be corrected for.

REFERENCES

1. Ankenbruck, Herman O., and Wolowicz, Chester H: Lateral Motions Encountered With The Douglas D-558-II All-Rocket Research Airplane During Exploratory Flights To a Mach Number of 2.0. NACA RM H54I27, 1954.

2. Weil, Joseph, Gates, Ordway B., Jr., Banner, Richard D., and Kuhl, Albert E.: Flight Experience of Inertia Coupling in Rolling Maneuvers. NACA RM H55E17b, 1955.

3. Gates, Ordway B., Jr., Weil, Joseph, and Woodling, C. H.: Effect of Automatic Stabilization on the Sideslip and Angle-of-Attack Disturbances in Rolling Maneuvers. NACA RM L55E25b, 1955.

4. Campbell, John P., and Woodling, Carroll H.: Calculated Effects of the Lateral Acceleration Derivatives on the Dynamic Lateral Stability of a Delta-Wing Airplane. NACA RM L54K26, 1955.

5. Campbell, John P., and McKinney, Marion O., Jr.: A Study of the Problem of Designing High-Speed Airplanes With Satisfactory Inherent Damping of the Dutch Roll Oscillation. NACA Rep. 1199, 1954. (Supersedes NACA TN 3035.)

6. Boatright, William B.: Wind-Tunnel Measurements of the Dynamic Cross Derivative $C_{l_r} - C_{l_{\dot\beta}}$ (Rolling Moment Due to Yawing Velocity and to Acceleration in Sideslip) of the Douglas D-558-II Airplane and Its Components at Supersonic Speeds Including Description of the Technique. NACA RM L55H16, 1955.

7. Beam, Benjamin H.: A Wind-Tunnel Test Technique for Measuring the Dynamic Rotary Stability Derivatives Including the Cross Derivatives at High Mach Numbers. NACA TN 3347, 1955.

8. Lessing, Henry C., Fryer, Thomas B., and Mead, Merriel H.: A System for Measuring the Dynamic Lateral Stability Derivatives in High-Speed Wind Tunnels. NACA TN 3348, 1954.

9. Mitchell, Jesse L., and Peck, Robert F.: Investigation of the Lateral Stability Characteristics of the Douglas X-3 Configuration at Mach Numbers From 0.6 to 1.1 by Means of a Rocket-Propelled Model. NACA RM L54L20, 1955.

10. D'Aiutolo, Charles T., and Henning, Allen B.: Lateral Characteristics at Low Lift Between Mach Numbers of 0.85 and 1.15 of a Rocket-Propelled Model of a Supersonic Airplane Configuration Having a Tapered Wing With Circular-Arc Sections and 40° Sweepback. NACA RM L55A31, 1955.

11. Larrabee, E. E.: Application of the Time Vector Method to the Analysis of Flight Test Lateral Oscillation Data. FRM No. 189, Cornell Aero. Lab., Inc., Sept. 9, 1953.

12. Wolowicz, Chester H.: Time-Vector Determined Lateral Derivatives of a Swept-Wing Fighter-Type Airplane With Three Different Vertical Tails at Mach Numbers Between 0.70 and 1.48. NACA RM H56C20, 1956.

13. Parks, James H.: Experimental Evidence of Sustained Coupled Longitudinal and Lateral Oscillations From a Rocket-Propelled Model of a 35° Swept Wing Airplane Configuration. NACA RM L54D15, 1954.

14. Michael, William H., Jr.: Analysis of the Effects of Wing Interference on the Tail Contributions to the Rolling Derivatives. NACA Rep. 1086, 1952. (Supersedes NACA TN 2332.)

15. Campbell, John P., and McKinney, Marion O.: Summary of Methods for Calculating Dynamic Lateral Stability and Response and for Estimating Lateral Stability Derivatives. NACA Rep. 1098, 1952. (Supersedes NACA TN 2409.)

16. Margolis, Kenneth: Theoretical Calculations of the Lateral Force and Yawing Moment Due to Rolling at Supersonic Speeds for Sweptback Tapered Wings With Streamwise Tips. Subsonic Leading Edges. NACA TN 2122, 1950.

17. Kuhn, Richard E., and Wiggins, James W.: Wind-Tunnel Investigation To Determine the Aerodynamic Characteristics in Steady Roll of a Model at High Subsonic Speeds. NACA RM L52K24, 1953.

18. Goodman, Alex: Effects of Wing Position and Horizontal-Tail Position on the Static Stability Characteristics of Models With Unswept and 45° Sweptback Surfaces With Some Reference to Mutual Interference. NACA TN 2504, 1951.

19. Purser, Paul E.: An Approximation to the Effect of Geometric Dihedral on the Rolling Moment Due to Sideslip for Wings at Transonic and Supersonic Speeds. NACA RM L52B01, 1952.

20. Gillis, Clarence L., and Chapman, Rowe, Jr.: Summary of Pitch-Damping Derivatives of Complete Airplane and Missile Configurations as Measured in Flight at Transonic and Supersonic Speeds. NACA RM L52K20, 1953.

21. D'Aiutolo, Charles T., and Henning, Allen B.: Lateral Stability Characteristics Between Mach Numbers of 0.80 and 1.57 and Simulation of Coupled Motion at Mach Number 1.30 of a Rocket-Propelled Model of an Airplane Configuration Having Thin Highly Tapered 45° Sweptback Surfaces. NACA RM L56A17, 1956.

22. Spearman, M. Leroy, Driver, Cornelius, and Hughes, William C.: Investigation of Aerodynamic Characteristics in Pitch and Sideslip of a 45° Sweptback-Wing Airplane Model With Various Vertical Locations of Wing and Horizontal Tail - Basic-Data Presentation, M = 2.01. NACA RM L54L06, 1955.

23. King, Thomas J., Jr.: Wind-Tunnel Investigation at High Subsonic Speeds of Some Effects of Fuselage Cross-Section Shape and Wing Height on the Static Longitudinal and Lateral Stability Characteristics of a Model Having a 45° Swept Wing. NACA RM L55J25, 1956.

24. DeYoung, John: Theoretical Antisymmetric Span Loading for Wings of Arbitrary Plan Form at Subsonic Speeds. NACA Rep. 1056, 1951. (Supersedes NACA TN 2140.)

25. Spearman, M. Leroy: Investigation of the Aerodynamic Characteristics in Pitch and Sideslip of a 45° Sweptback-Wing Airplane Model With Various Vertical Locations of the Wing and Horizontal Tail - Effect of Wing Location and Geometric Dihedral for the Wing-Body Combination, M = 2.01. NACA RM L55B18, 1955.

26. Mangler, K. W.: Calculation of the Pressure Distribution Over a Wing at Sonic Speeds. R. & M. No. 2888, British A.R.C., Sept. 1951.

27. McDearmon, Russell W., and Heinke, Harry S., Jr.: Investigations of the Damping In Roll Of Swept and Tapered Wings at Supersonic Speeds. NACA RM L53A13, 1953.

28. Anon.: Military Specification - Flying Qualities of Piloted Airplanes. MIL-F-8785 (ASG), Sept. 1, 1954. (Amendment - 1, Oct. 19, 1954.)

29. Williams, Walter C., and Phillips, William H.: Some Recent Research on the Handling Qualities of Airplanes. NACA RM H55L29a, 1956.

30. Vitale, A. James: Effects of Wing Elasticity on the Aerodynamic Characteristics of an Airplane Configuration Having 45° Sweptback Wings as Obtained From Free-Flight Rocket-Model Tests at Transonic Speeds. NACA RM L52L30, 1953.

31. Queijo, M. J., and Riley, Donald R.: Calculated Subsonic Span Loads and Resulting Stability Derivatives of Unswept and 45° Sweptback Tail Surfaces in Sideslip and in Steady Roll. NACA TN 3245, 1954.

TABLE I

GEOMETRIC CHARACTERISTICS OF THE MODELS

Wing:
  Area (extended to model center line), sq ft 4.41
  Span, ft 4.20
  Aspect ratio 4.0
  Mean aerodynamic chord, ft 1.21
  Sweepback (quarter chord), deg 45
  Taper ratio 0.20
  Airfoil section . . . . NACA 65A004

Horizontal tail:
  Area (extended to model center line), sq ft 0.88
  Aspect ratio 4.0
  Span, ft 1.88
  Mean aerodynamic chord, ft 0.54
  Sweepback (quarter chord), deg 45
  Taper ratio 0.20
  Airfoil section . . . . NACA 65A004

Vertical tail:
  Area (extended to model center line), sq ft 0.89
  Aspect ratio 1.59
  Height (above center line of model), ft 1.19
  Sweepback (quarter chord), deg 45
  Taper ratio 0.17
  Airfoil section . . . . NACA 65A004

TABLE II

MASS AND INERTIA CHARACTERISTICS

	Model 1	Model 2	Model 3
Weight, lb	103.0	111.0	112.7
Center-of-gravity position, percent $\bar{c}$ . .	0	3.8	-0.6
Moments of inertia:			
Pitch, slug-ft^2	5.47	5.88	5.90
Yaw, slug-ft^2	5.81	6.14	6.38
Roll, slug-ft^2	0.61	0.66	0.69
Inclination of principal axis, deg . . .	2.15	0.75	1.60
Product of inertia	0.20	0.07	0.16

TABLE III

FUSELAGE ORDINATES

Station, in.	Diameter, in.
0	0
3	1.60
6	3.00
9	4.24
12	5.28
15	6.14
18	6.84
21	7.34
24	7.66
27.8	7.80
30	7.78
33	7.74
36	7.64
39	7.48
42	7.30
45	7.06
48	6.78
51	6.44
54	6.08
57	5.66
60	5.18
63	4.68
66	4.12
69.5	3.42

TABLE IV

ESTIMATED ACCURACY OF VARIOUS MEASURED QUANTITIES

[All increments may be positive or negative]

Quantity	Model	Accuracy at -	
		M = 1.3	M = 0.7
M, percent	1 and 2	1.0	3.0
q, percent	1 and 2	2.0	6.0
$T_{1/2}$, sec	1 and 2	.03	.10
P, sec	1 and 2	.005	.010
$\frac{p}{\beta}$, sec^{-1}	1	10	3
	2	4	2
Ω_p, deg	1	3	3
	2	6	10
W, percent	1 and 2	0.5	
k_z^2, percent	1 and 2	1.5	
k_x^2, percent	1 and 2	3.5	
ϵ, deg	1 and 2	.5	
α, deg	1 and 2	.5	
β, deg	1 and 2	.5	
$\frac{a_t}{\beta}$, percent	1 and 2	2.0	

TABLE V

CALCULATED ACCURACY OF AERODYNAMIC DERIVATIVES

$\left[\text{All increments may be positive or negative, and all derivatives are for } \beta \text{ in radians}\right]$

(a) Model 1

Increment due to error in -	ΔC_{Y_β} for -		ΔC_{n_β} for -		ΔC_{l_β} for -		ΔC_{l_p} for -		$\Delta\left(C_{n_r} - C_{n_{\dot\beta}}\right)$ for -	
	M = 1.3	M = 0.7	M = 1.3	M = 0.7	M = 1.3	M = 0.7	M = 1.3	M = 0.7	M = 1.3	M = 0.7
$\dfrac{W}{k_z^2}$	0.003 -----	0.002 -----	0.001 .002	0.001 .002	0.001 -----	0.001 -----	0.001 -----	0.002 -----	0.004 .006	0.004 .009
k_x^2	-----	-----	-----	-----	.004	.003	.008	.012	-----	-----
ϵ	-----	-----	.005	.004	.001	.001	0	0	.140	.113
α	-----	-----	.003	.005	0	0	0	0	.112	.052
$\dfrac{a_t}{\beta}$	.011	.009	0	0	0	0	0	0	0	0
q	.011	.028	.002	.008	.002	.006	.005	.020	.016	.052
$T_{1/2}$	-----	-----	0	0	0	.001	.003	.011	.021	.087
P	-----	-----	.004	.004	.003	.002	.005	.007	.010	.007
$\dfrac{p}{\beta}$	-----	-----	.001	0	.004	.004	0	.001	.034	.011
Ω_p	-----	-----	.001	.001	.005	.005	.023	.035	.033	.026
Omitting weight effects	-----	-----	0	0	0	0	0	0	.012	.006
Probable error, $\sqrt{\Sigma(\Delta)^2}$	.016	.029	.008	.011	.009	.010	.026	.044	.188	.163
Value of derivative	-.561	-.470	.119	.126	-.121	-.098	-.225	-.330	-.785	-.869
Probable error, percent of derivative	3	6	7	9	7	10	12	13	24	19
$C_{l_r} - C_{l_{\dot\beta}}$ (100 percent error)	-----	-----	-----	-----	.002	.003	.013	.022	------	------
C_{n_p} (100 percent error)	-----	-----	.004	.003	-----	-----	-----	-----	.155	.090

TABLE V.- CONCLUDED

CALCULATED ACCURACY OF AERODYNAMIC DERIVATIVES

(b) Model 2

Increment due to error in -	ΔC_{Y_β}		ΔC_{n_β}		ΔC_{l_β}		$\Delta\left(C_{l_r} - C_{l_{\dot\beta}}\right)$		$\Delta\left(C_{n_r} - C_{n_{\dot\beta}}\right)$	
	M = 1.3	M = 0.7	M = 1.3	M = 0.7	M = 1.3	M = 0.7	M = 1.3	M = 0.7	M = 1.3	M = 0.7
W	0.004	0.004	0.001	0.001	0	0	0	0	0.002	0.003
$k_z{}^2$	-----	-----	.003	.004	-----	-----	-----	-----	.006	.008
$k_x{}^2$	-----	-----	-----	-----	0	0	.006	.003	-----	-----
ϵ	-----	-----	0	0	.001	.002	.004	.004	0	.016
α	-----	-----	0	0	0	0	0	0	.020	.016
$\dfrac{a_t}{\beta}$	.018	.014	0	0	0	0	0	0	0	0
q	.018	.043	.004	.014	0	.001	.002	.006	.008	.032
$T_{1/2}$	-----	-----	0	0	0	0	.001	.002	.063	.093
P	-----	-----	.015	.015	.001	.001	.004	.005	.020	.039
$\dfrac{p}{\beta}$	-----	-----	0	0	.002	.003	.020	.019	0	0
Ω_p	-----	-----	0	0	.001	0	.034	.036	0	.010
Omitting weight effect	-----	-----	0	0	0	0	0	0	0	0
Probable error, $\sqrt{\Sigma(\Delta)^2}$	.026	.045	.016	.021	.003	.004	.040	.042	.070	.108
Value of derivative	-.877	-.716	.212	.241	-.017	-.020	.120	.100	-.420	-.540
Error, percent of derivative	3	6	8	9	18	20	33	42	17	20
C_{l_p} (0.05 error)	-----	-----	-----	-----	.001	.001	.020	.020	------	------
C_{n_p} (100 percent error)	-----	-----	.001	.001	------	------	------	------	.013	.020

(a) High-wing model.
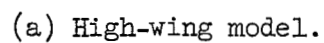
Figure 1.- Three-view drawing of the models. All dimensions are in inches.
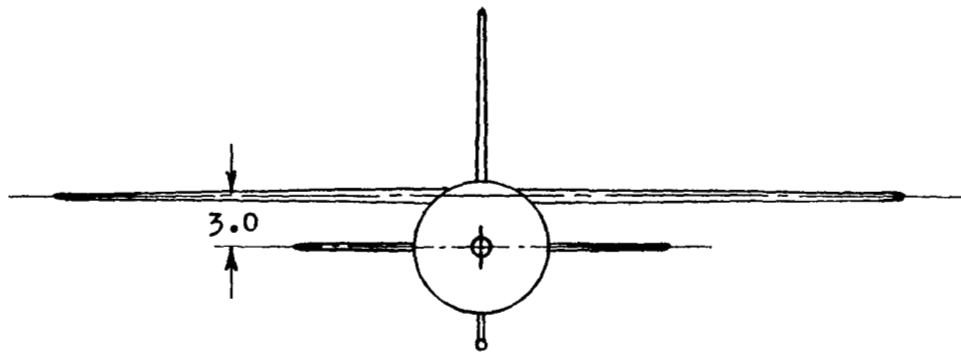
Model 1
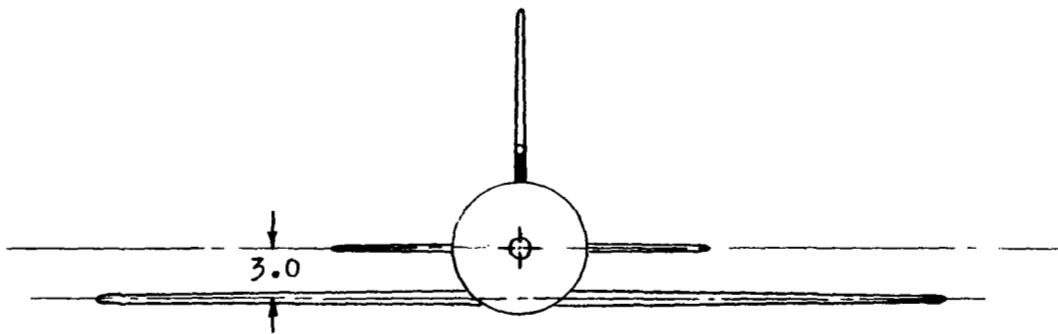
Model 2
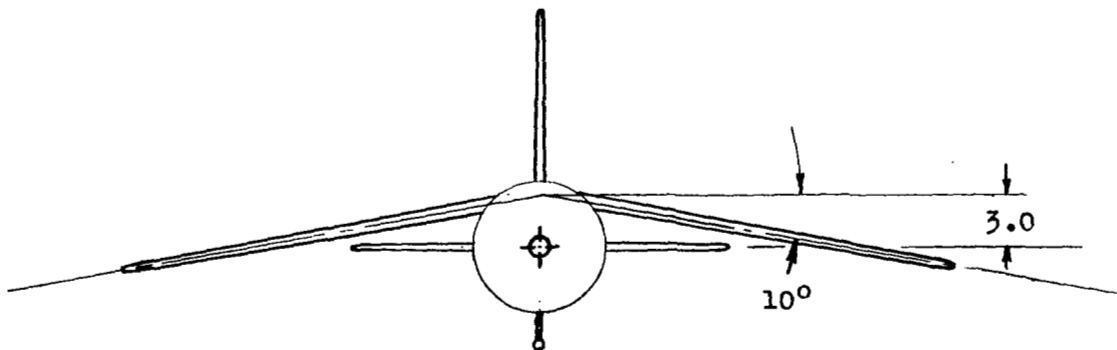
Model 3

(b) Front views of models.

Figure 1.- Concluded.
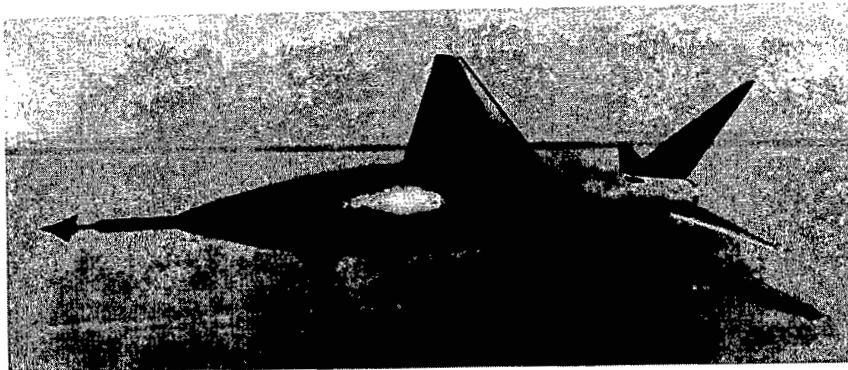
. Model I
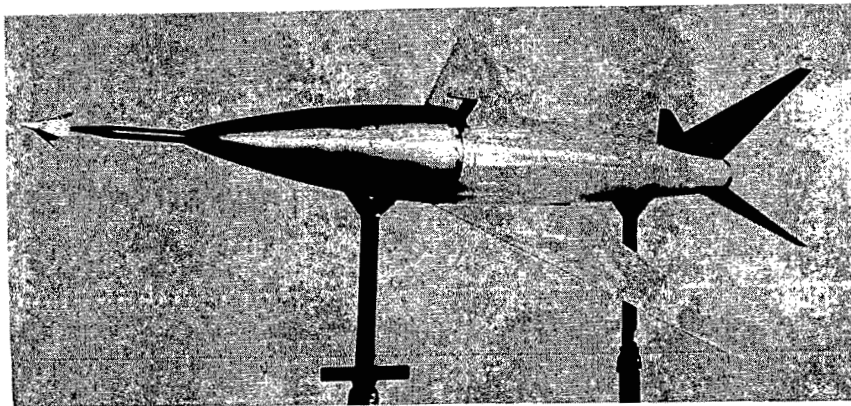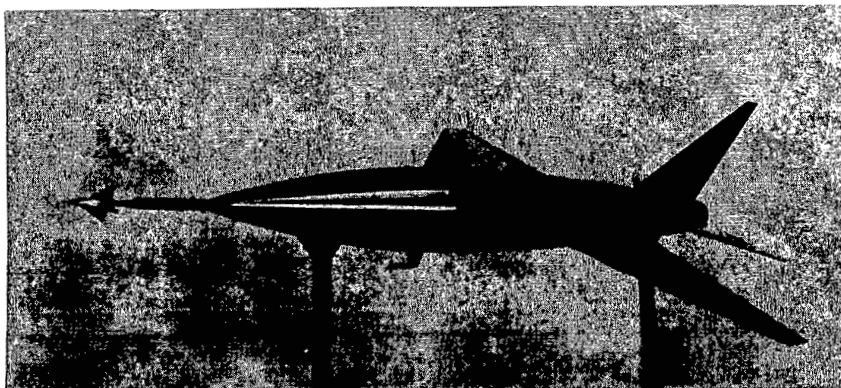
Model 2

Model 3

(a) Sideviews.   L-93517

Figure 2.- Photographs of the models.
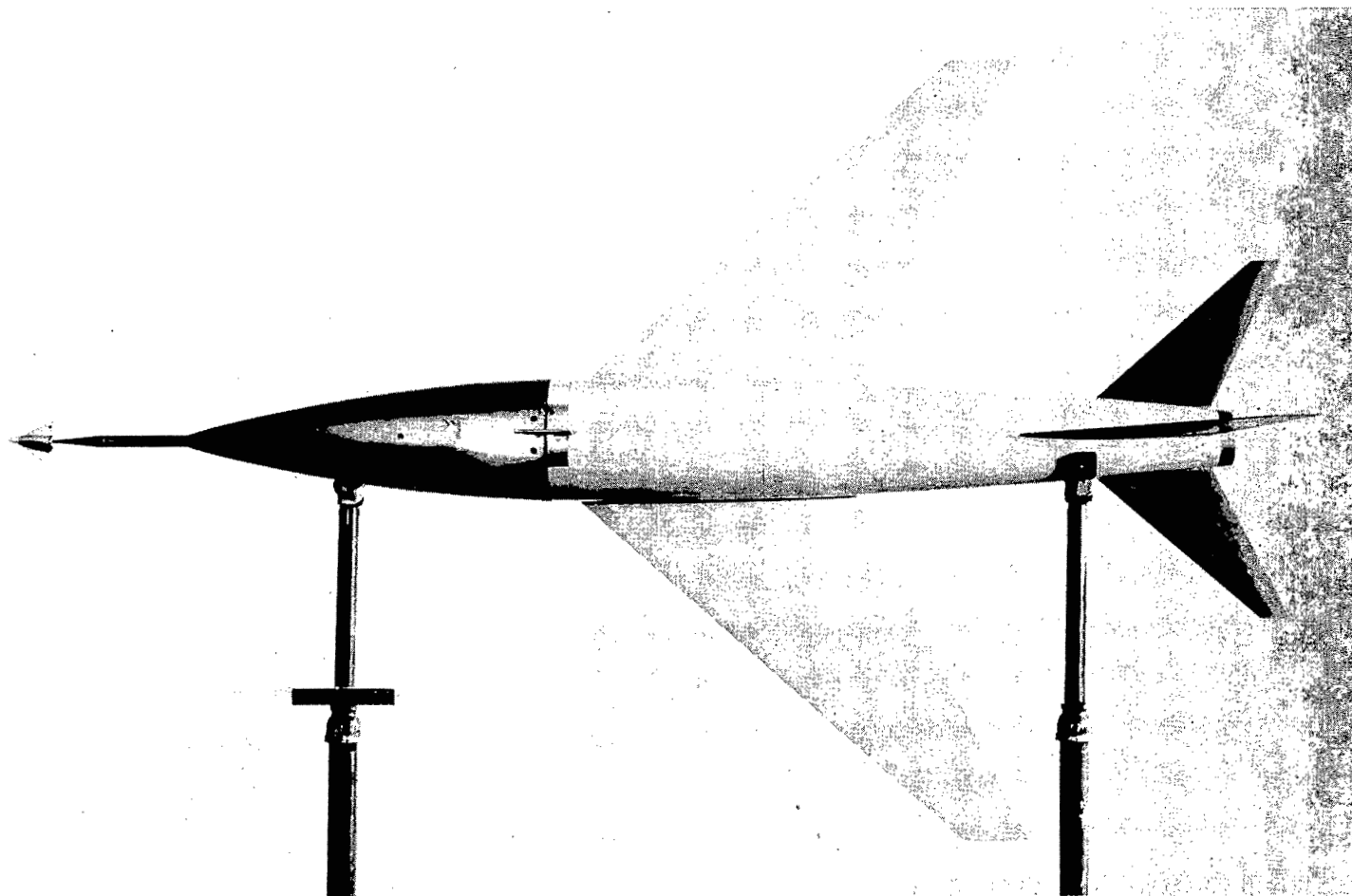
(b) Plan view of model 2.

L-93515

Figure 2.- Continued.
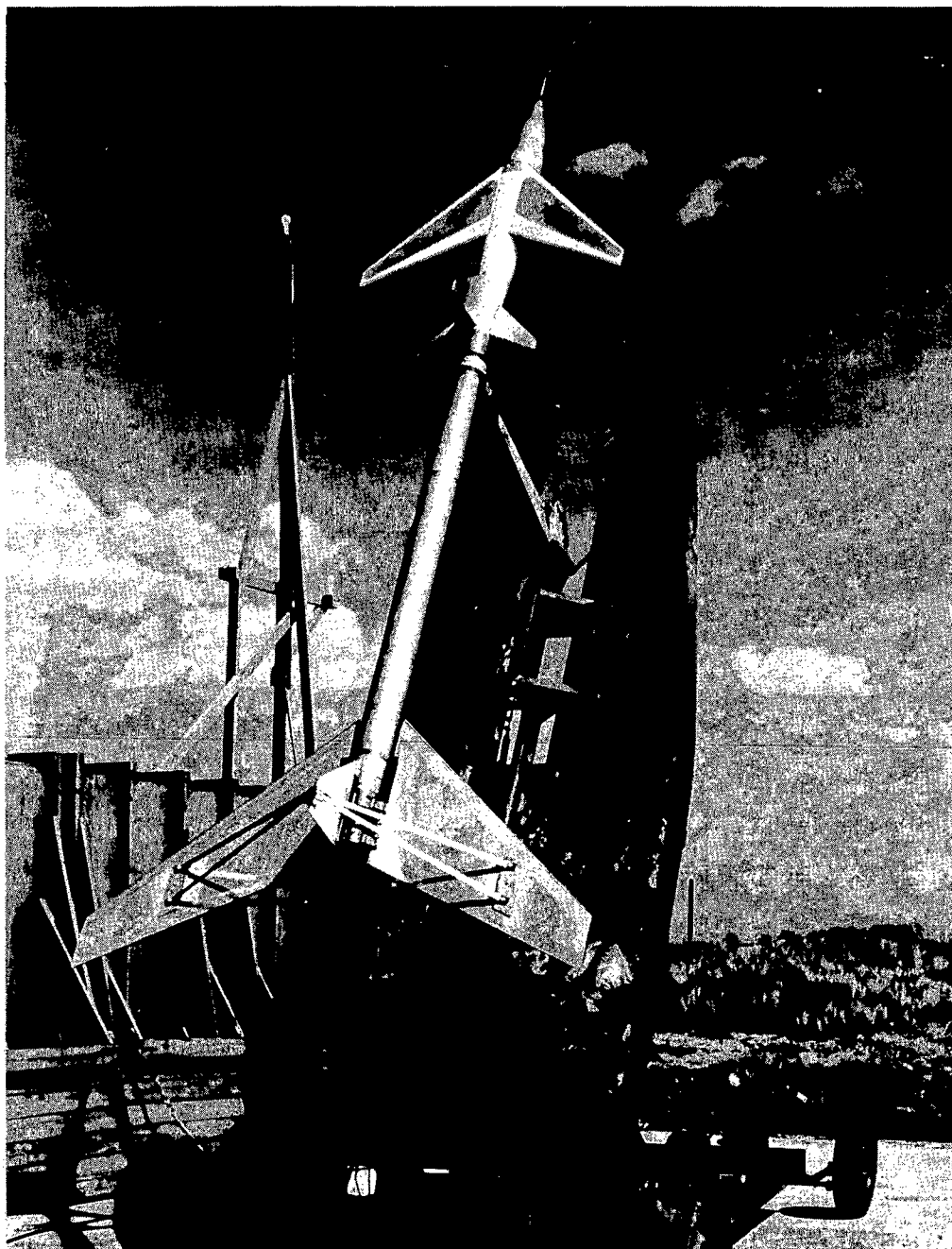
(c) Model 1 on the launcher.   L-93516

Figure 2.- Concluded.
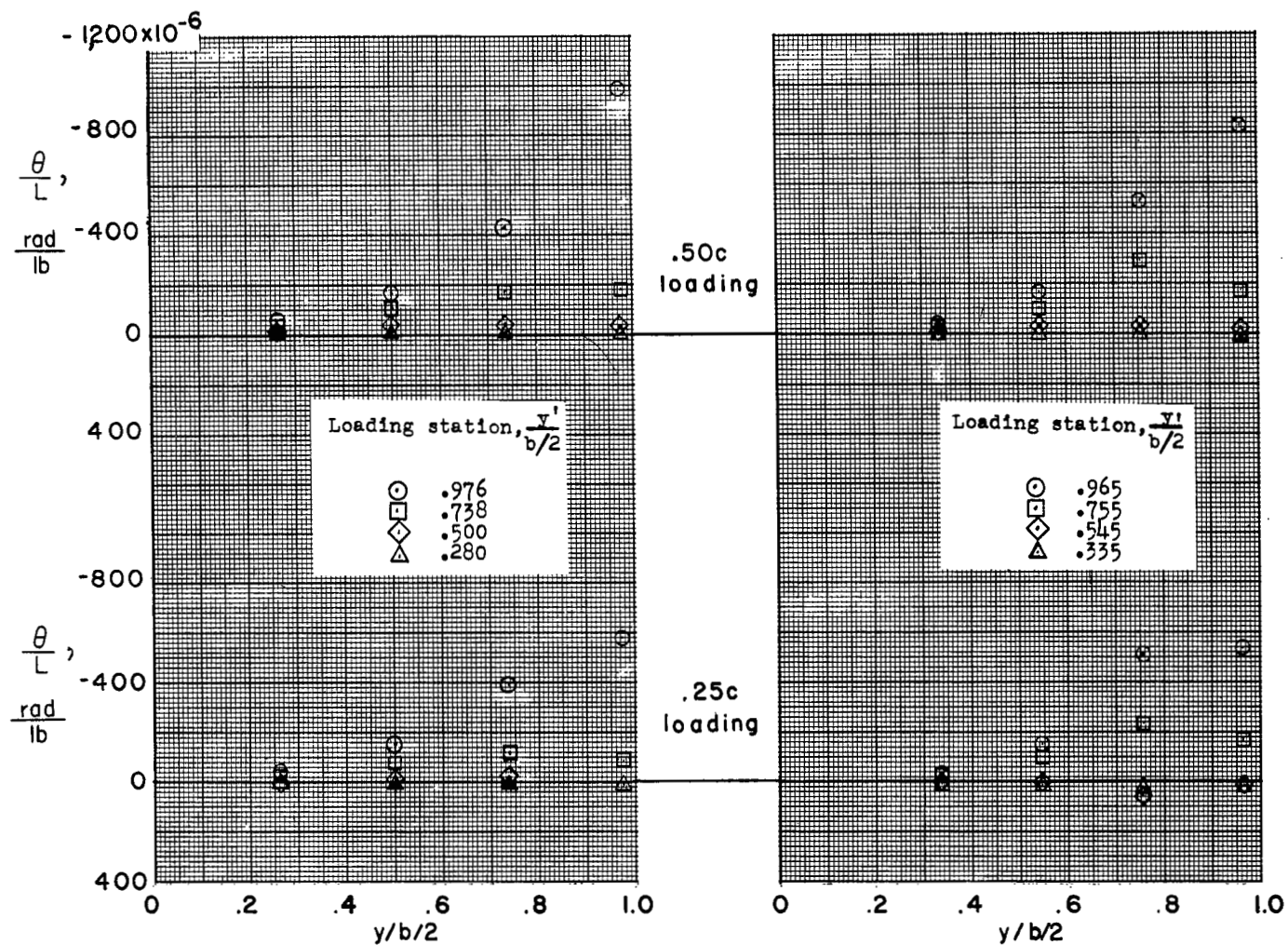
(a) Wing.

(b) Vertical tail.

Figure 3.- Measured influence coefficients.
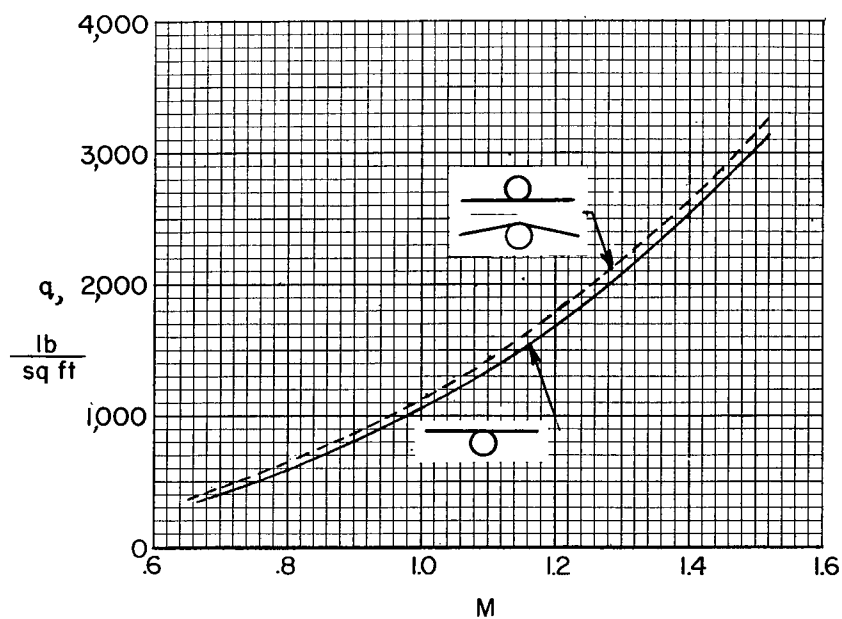
(a) Dynamic pressure.
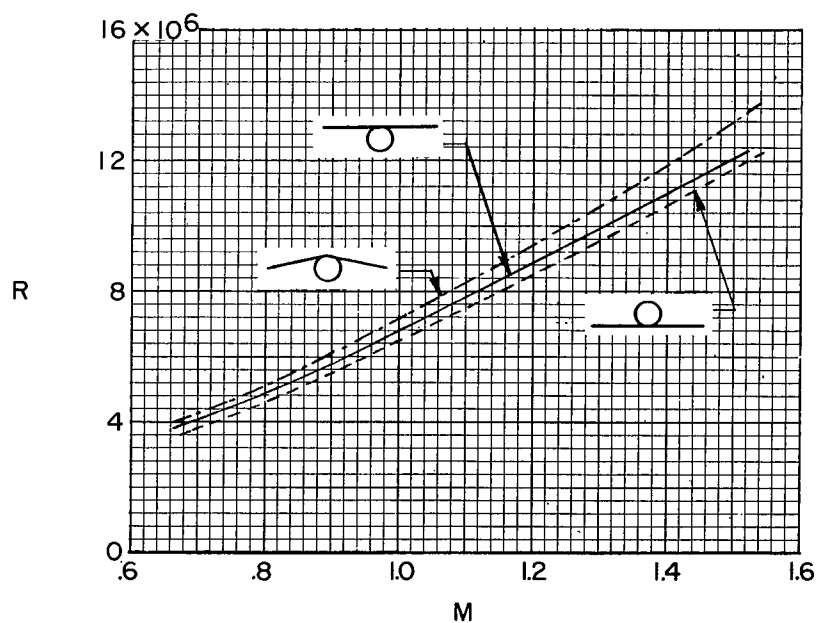
(b) Reynolds number based on mean aerodynamic chord.

Figure 4.- Test conditions.
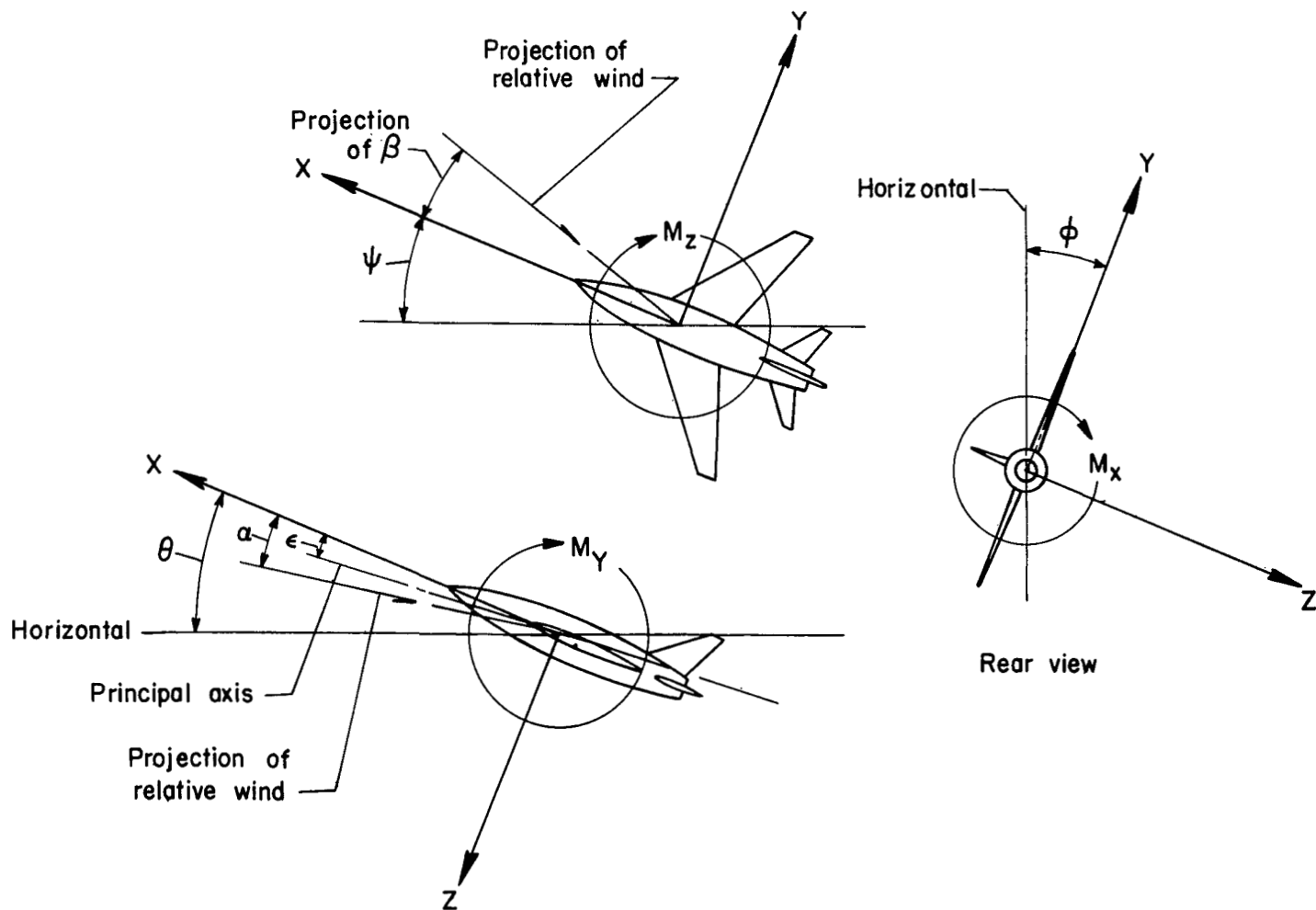
Figure 5.- System of axes.
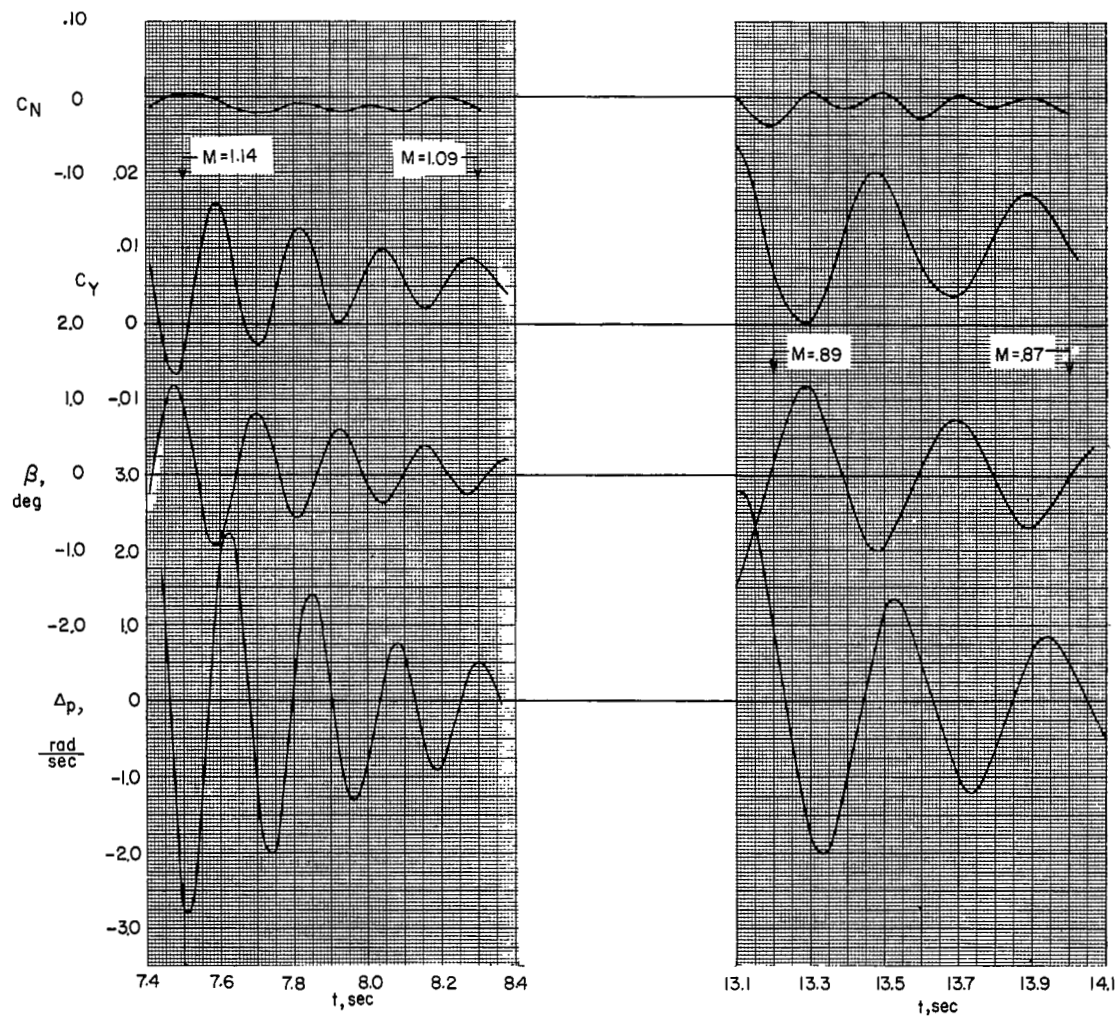
(a) Supersonic oscillation.

(b) Subsonic oscillation.

Figure 6.- Time history of model 1.
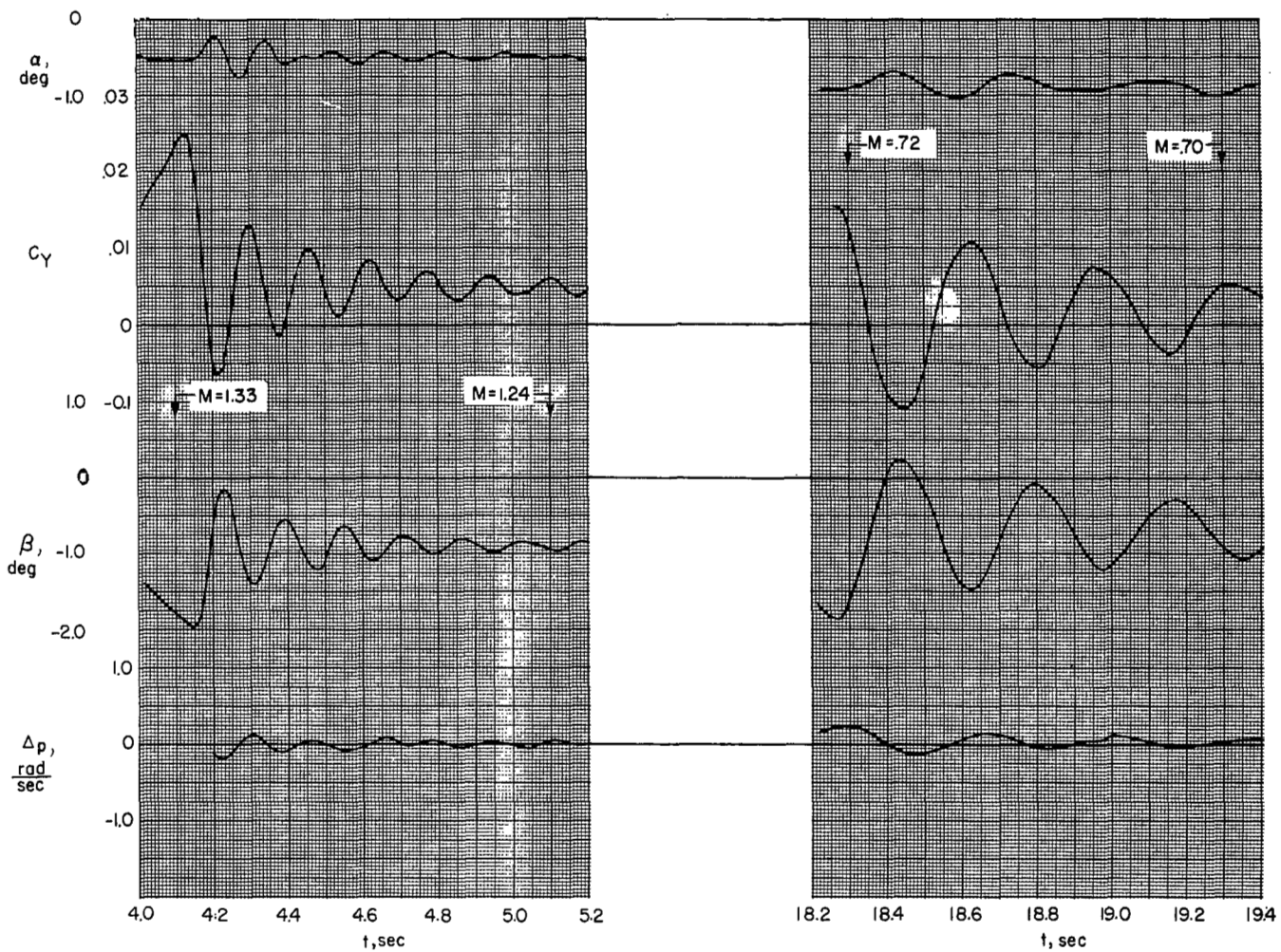
(a) Supersonic oscillation.

(b) Subsonic oscillation.

Figure 7.- Time history of model 2.
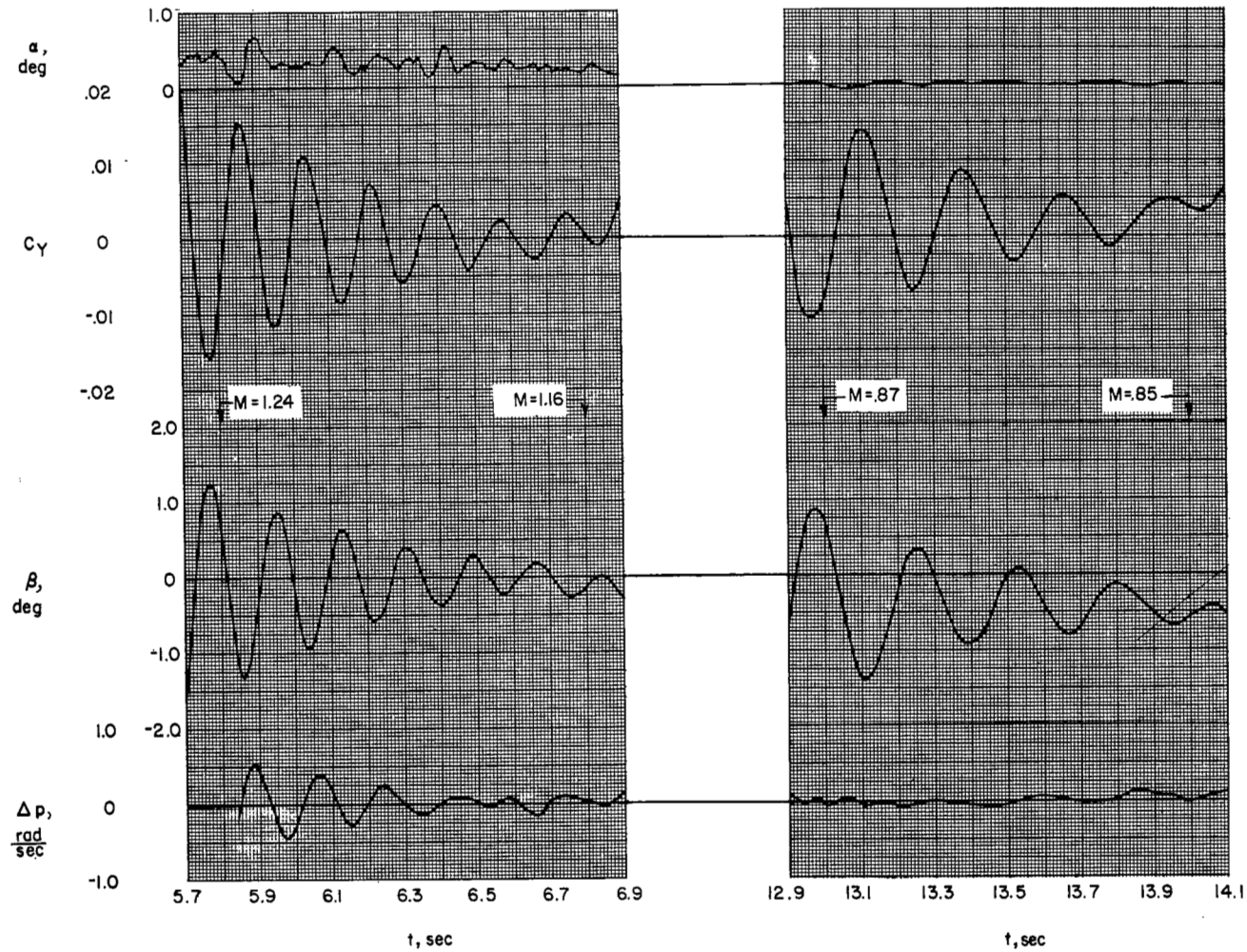
(a) Supersonic oscillation.　　　　(b) Subsonic oscillation.

Figure 8.- Time history of model 3.

$$\frac{mV}{qS}\left|\frac{\dot\beta}{\beta}\right| + \frac{mV}{qS}\left|\frac{r}{\beta}\right| - \frac{mV}{qS}\,\alpha\,\left|\frac{p}{\beta}\right| - \left|\frac{C_y}{\beta}\right| = 0$$
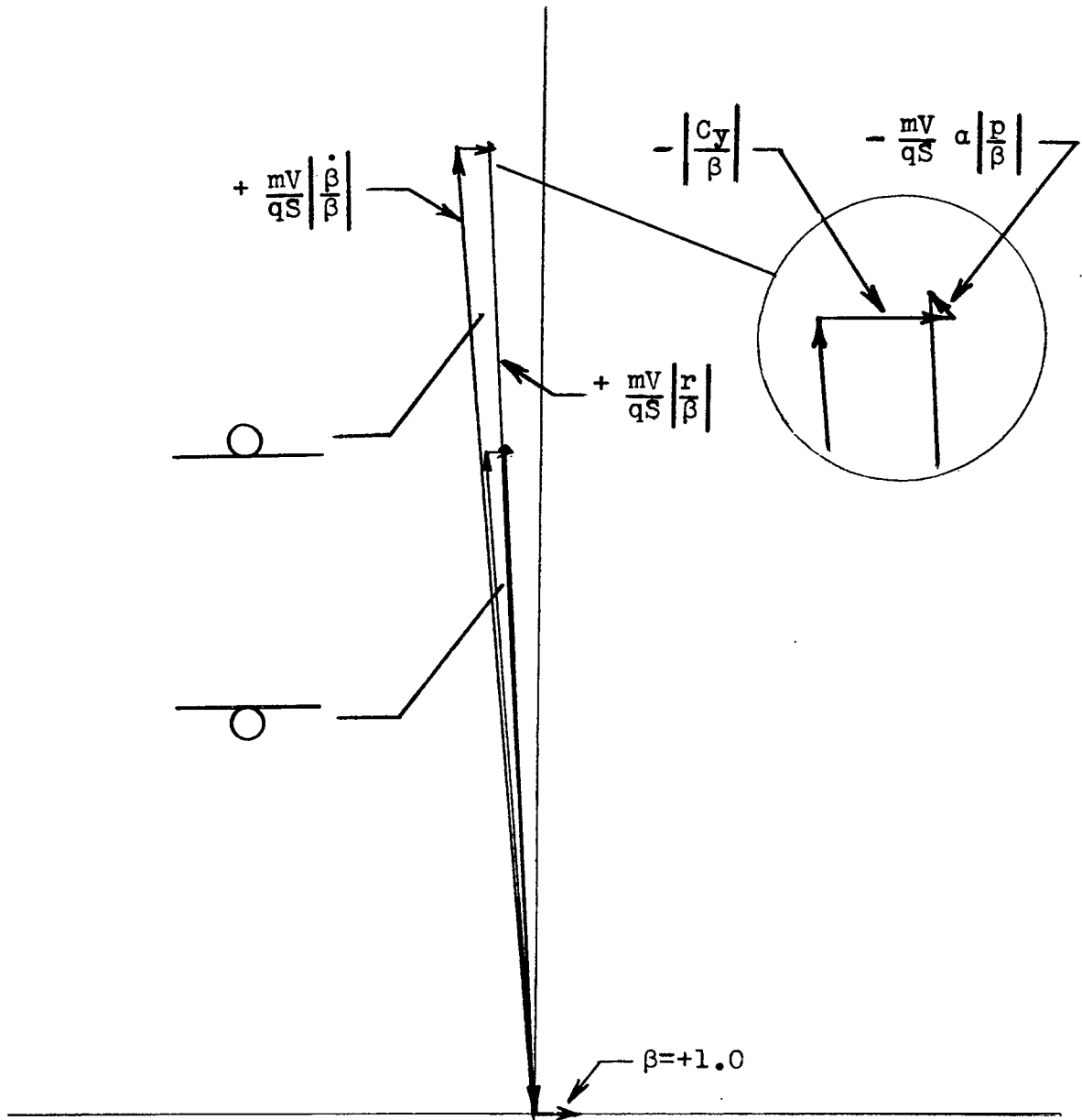
(a) Side-force diagram.

Figure 9.- Vector diagrams for high-wing and low-wing models. M ≈ 1.2.

$$\frac{I_x}{q Sb}\left|\frac{\dot{p}}{\beta}\right| - \frac{I_{xz}}{q Sb}\left|\frac{\dot{r}}{\beta}\right| - c_{l\beta} - c_{lp}\frac{b}{2V}\left|\frac{p}{\beta}\right| - \left(c_{lr} - c_{l\dot{\beta}}\right)\frac{b}{2V}\left|\frac{r}{\beta}\right| = 0$$
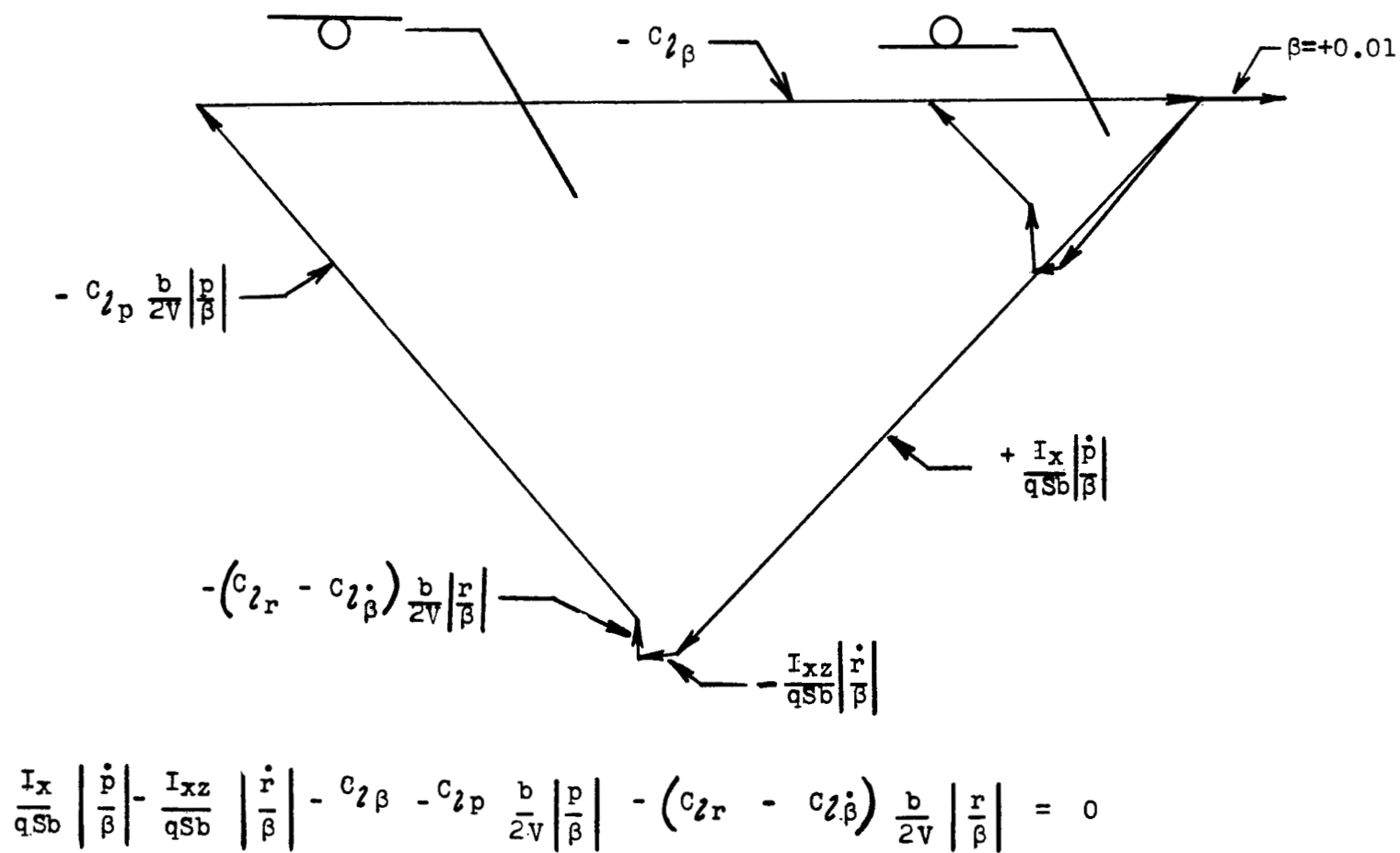
(b) Rolling-moment diagram.

Figure 9.- Continued.

$$\frac{I_z}{qSb}\left|\frac{\dot{r}}{\beta}\right| - \frac{I_{xz}}{qSb}\left|\frac{\dot{p}}{\beta}\right| - c_{n_\beta} - c_{n_p}\frac{b}{2V}\left|\frac{p}{\beta}\right| - \left(c_{n_r} - c_{n_{\dot{\beta}}}\right)\frac{b}{2V}\left|\frac{r}{\beta}\right| = 0$$
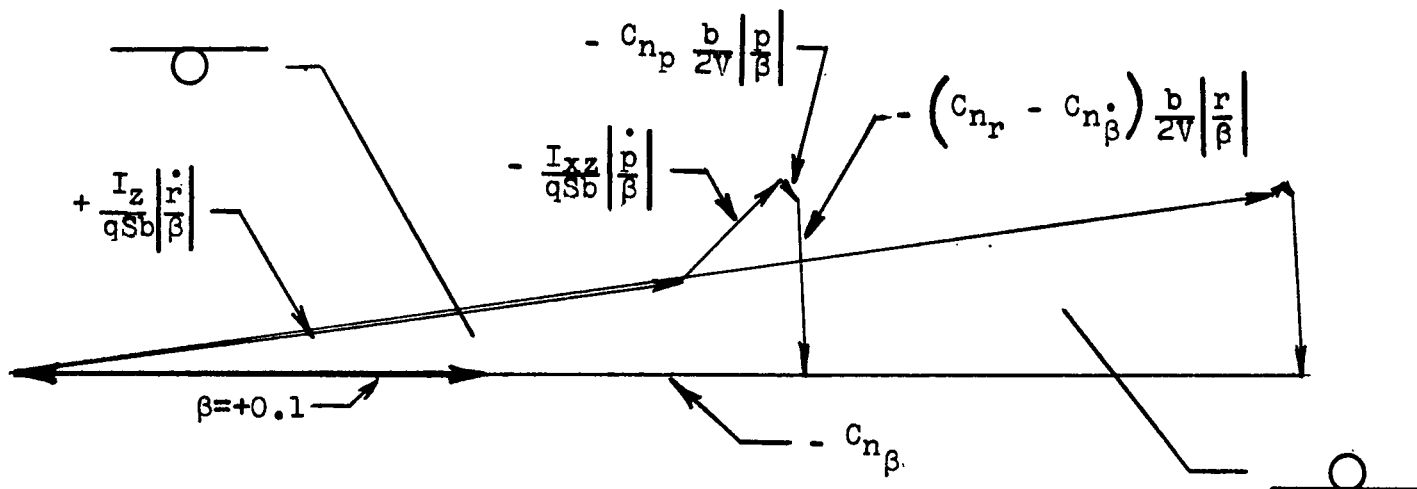
(c) Yawing-moment diagram.

Figure 9.- Concluded.
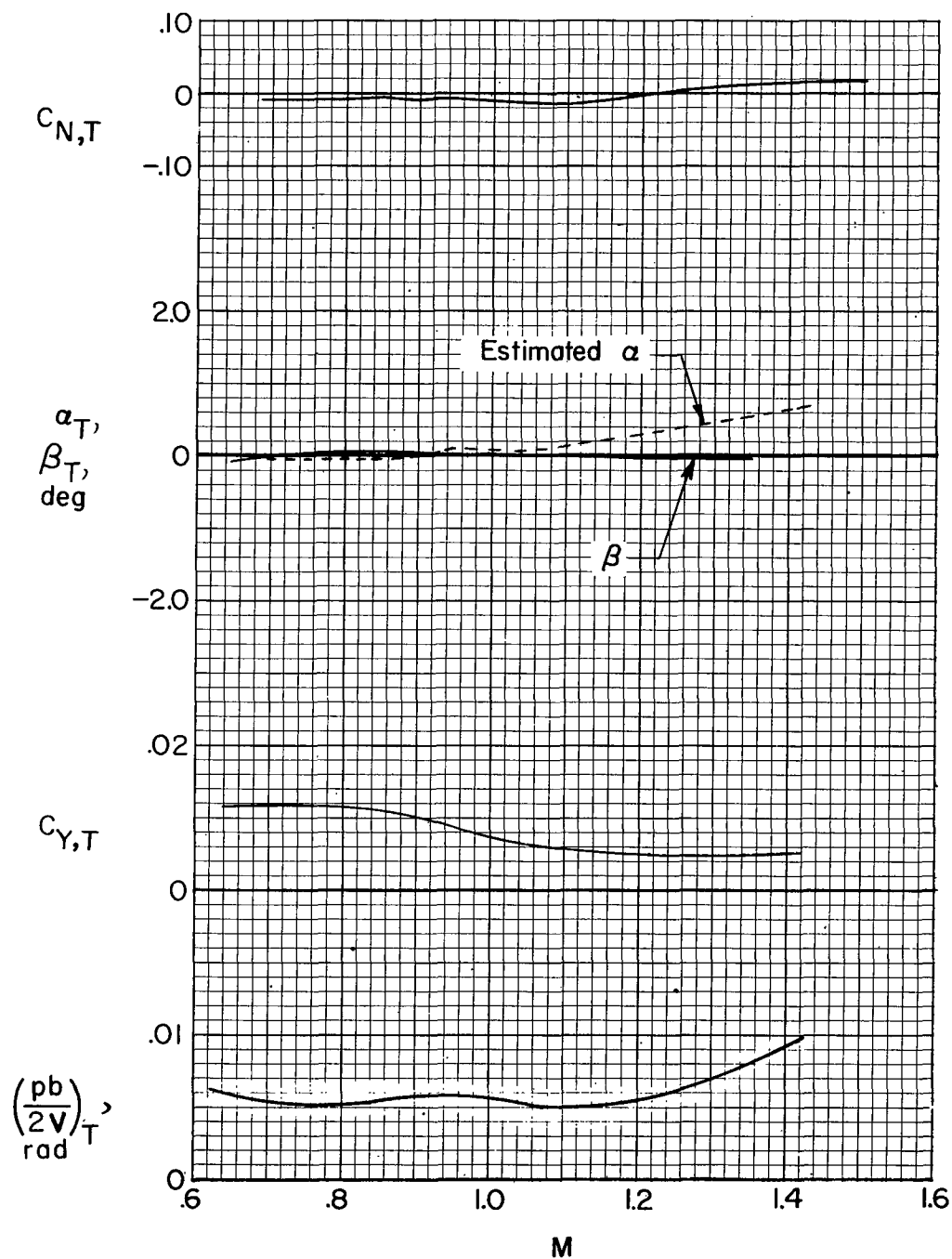
(a) Model 1. High-wing model.

Figure 10.- Model trim characteristics.
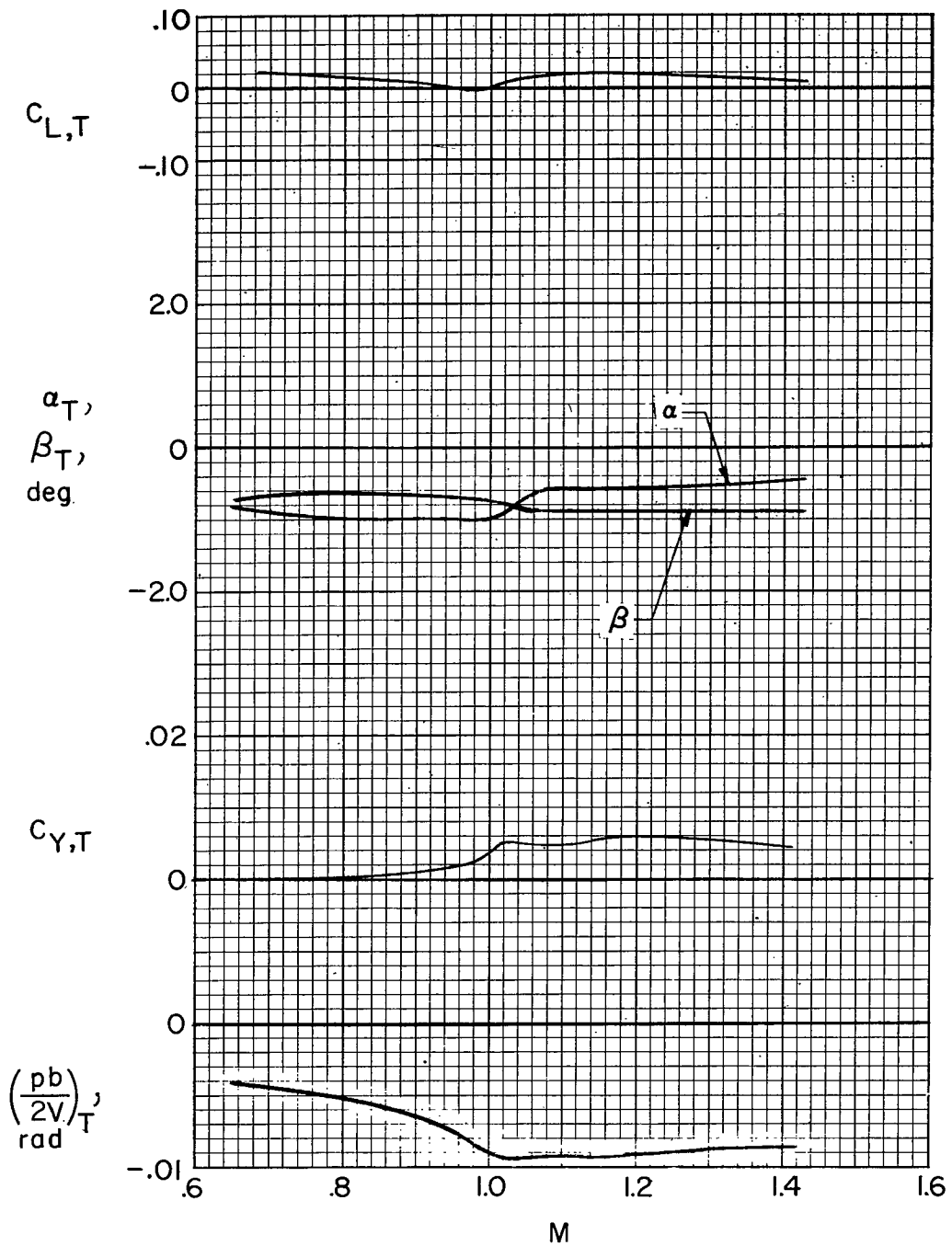
(b) Model 2.   Low-wing model.

Figure 10.- Continued.
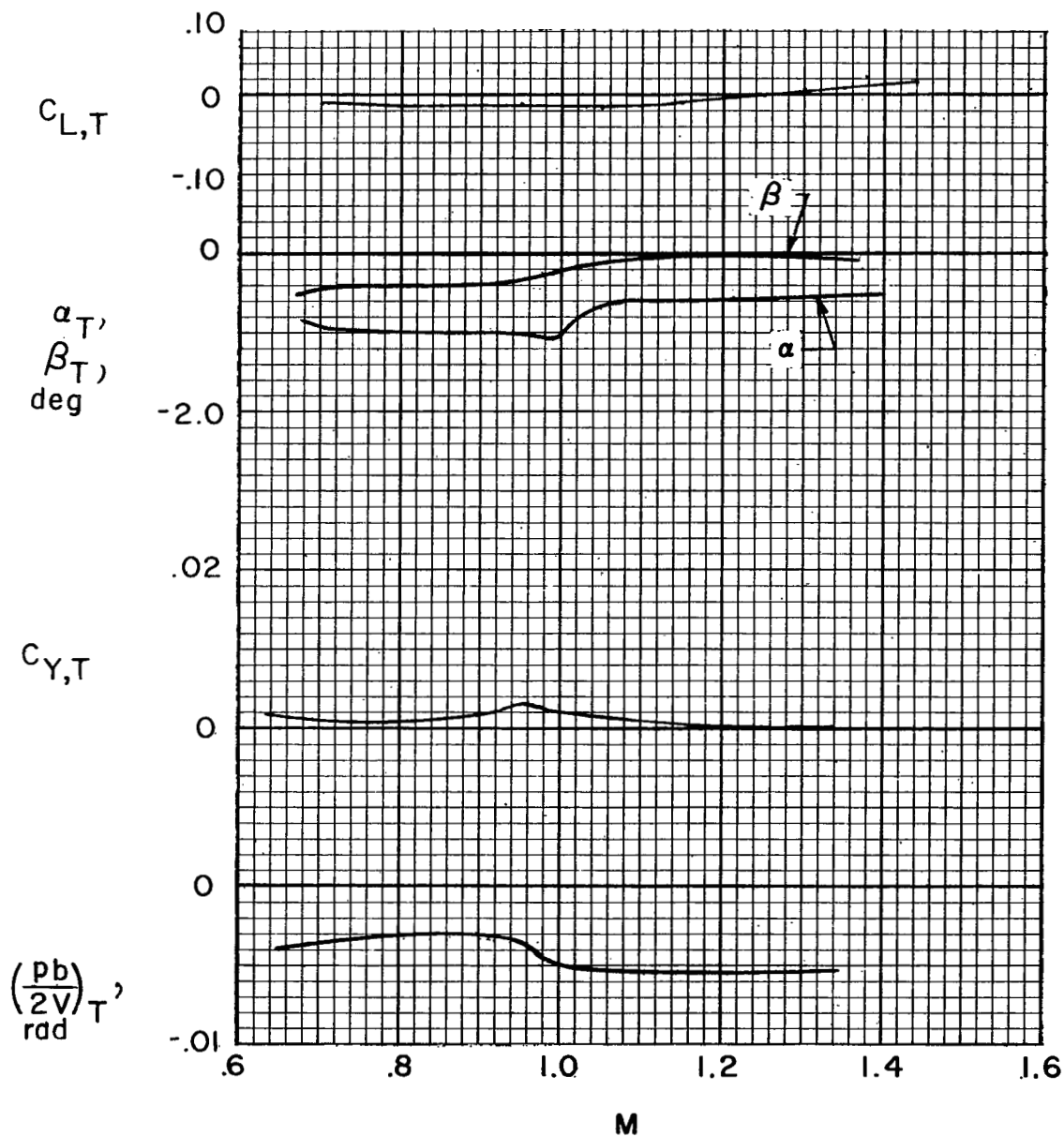
(c) Model 3. High-wing model, 10° cathedral.

Figure 10.- Concluded.
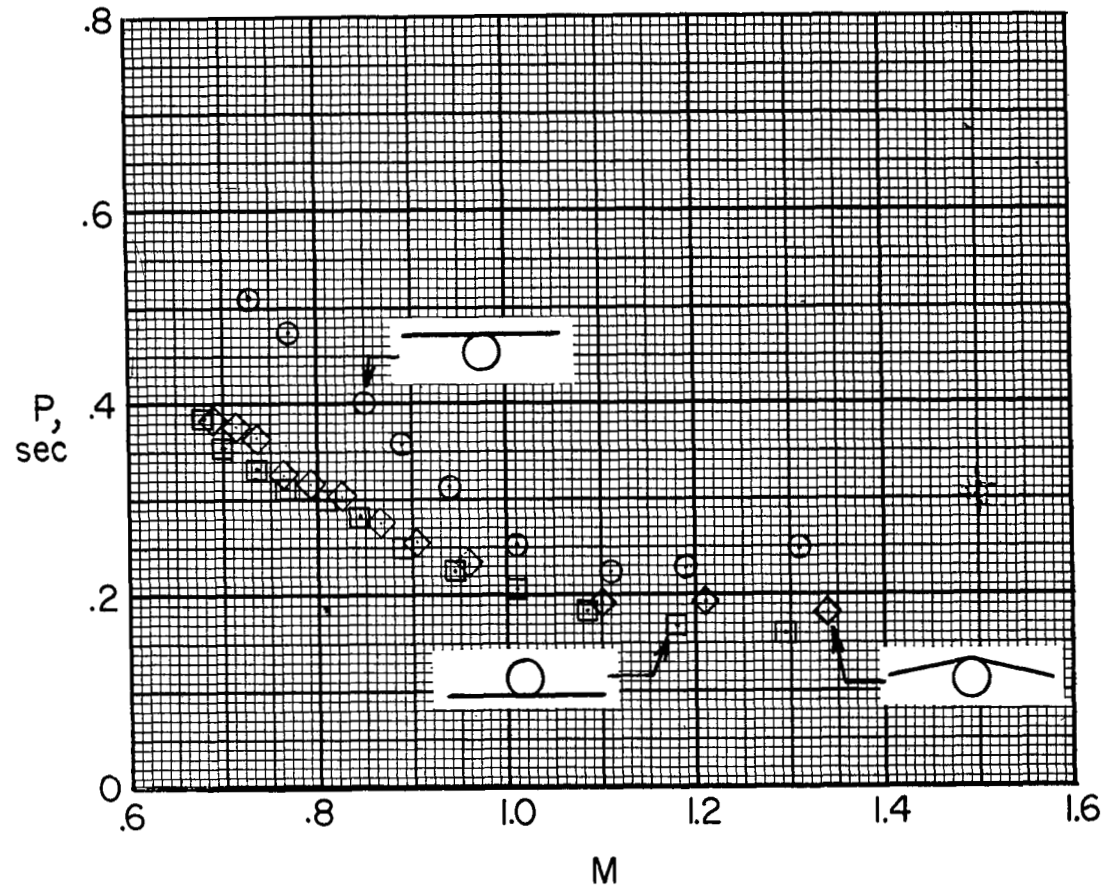
Figure 11.- Period of the oscillation.
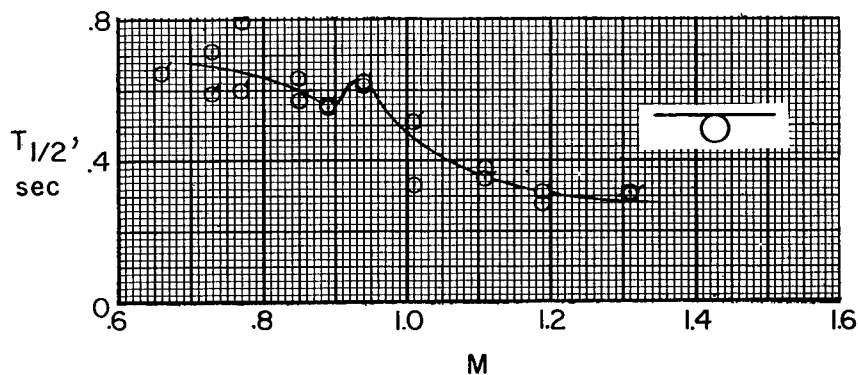
(a) Model 1. High wing.
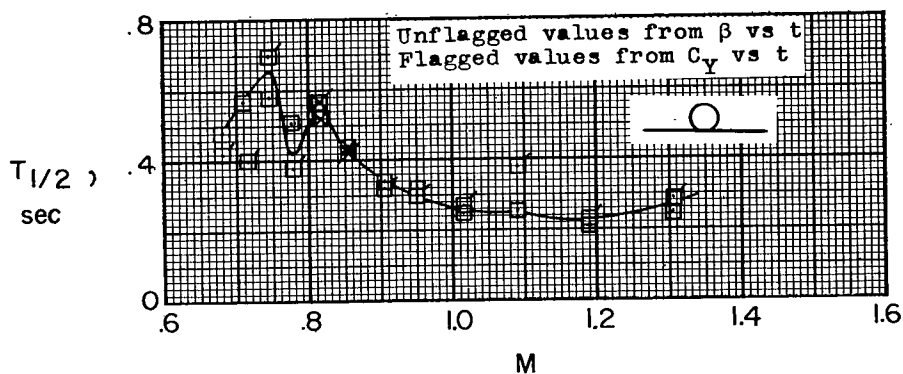
(b) Model 2. Low-wing model.
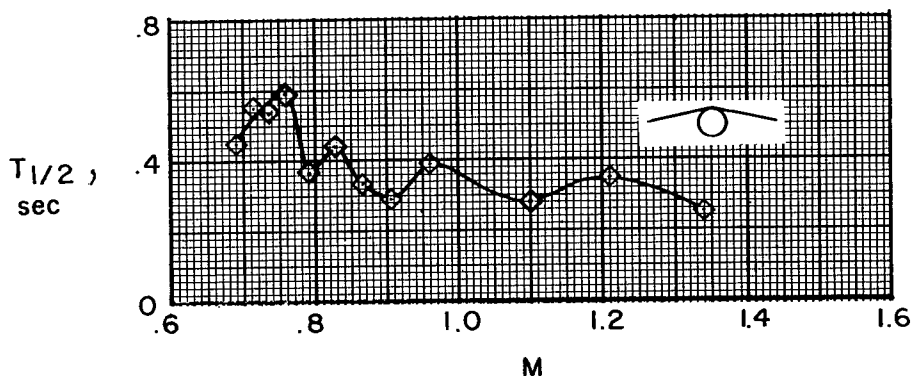
(c) Model 3. High-wing model, 10° cathedral.

Figure 12.- Time to damp to one-half amplitude.
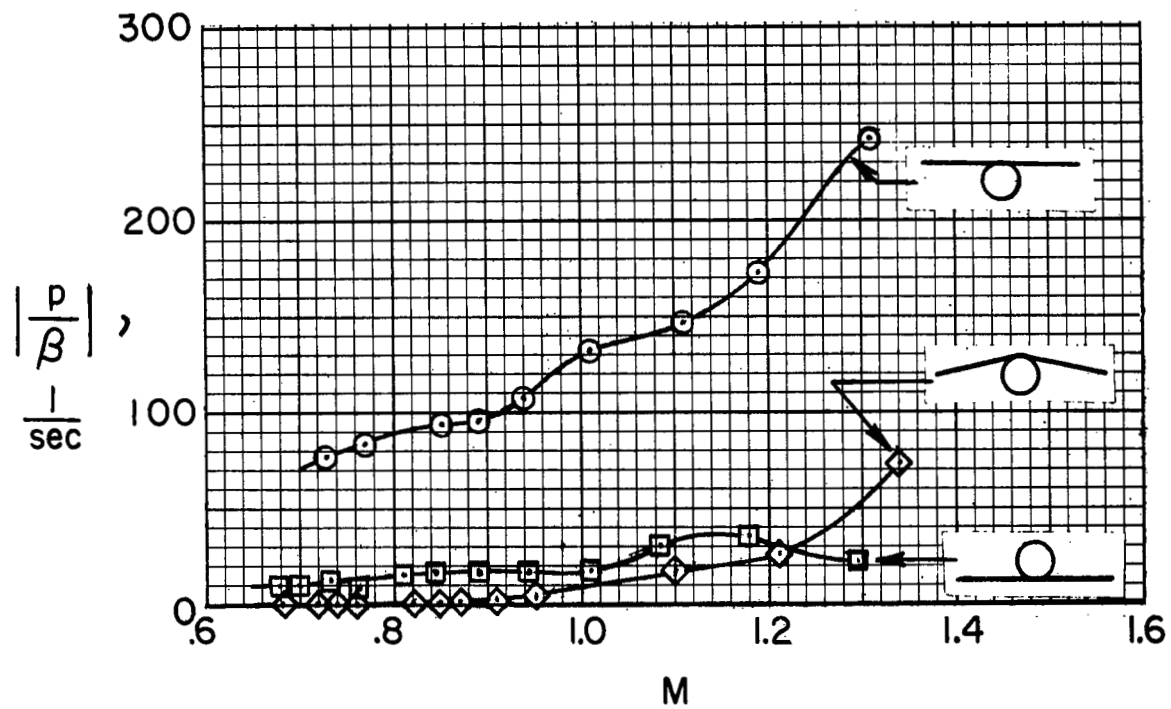
Figure 13.- Roll-velocity amplitude.
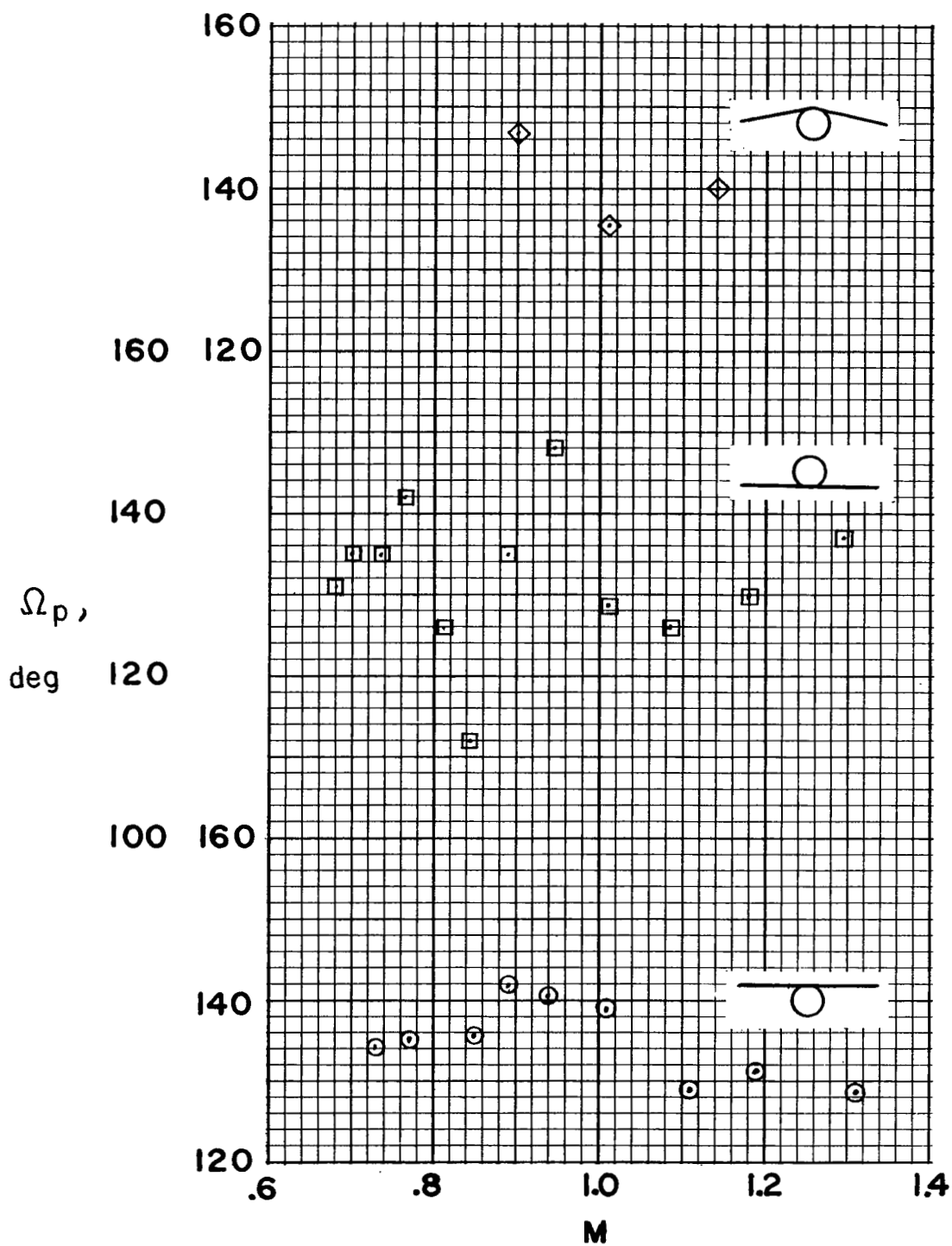
Figure 14.- Phase angle between rolling velocity and sideslip angle.
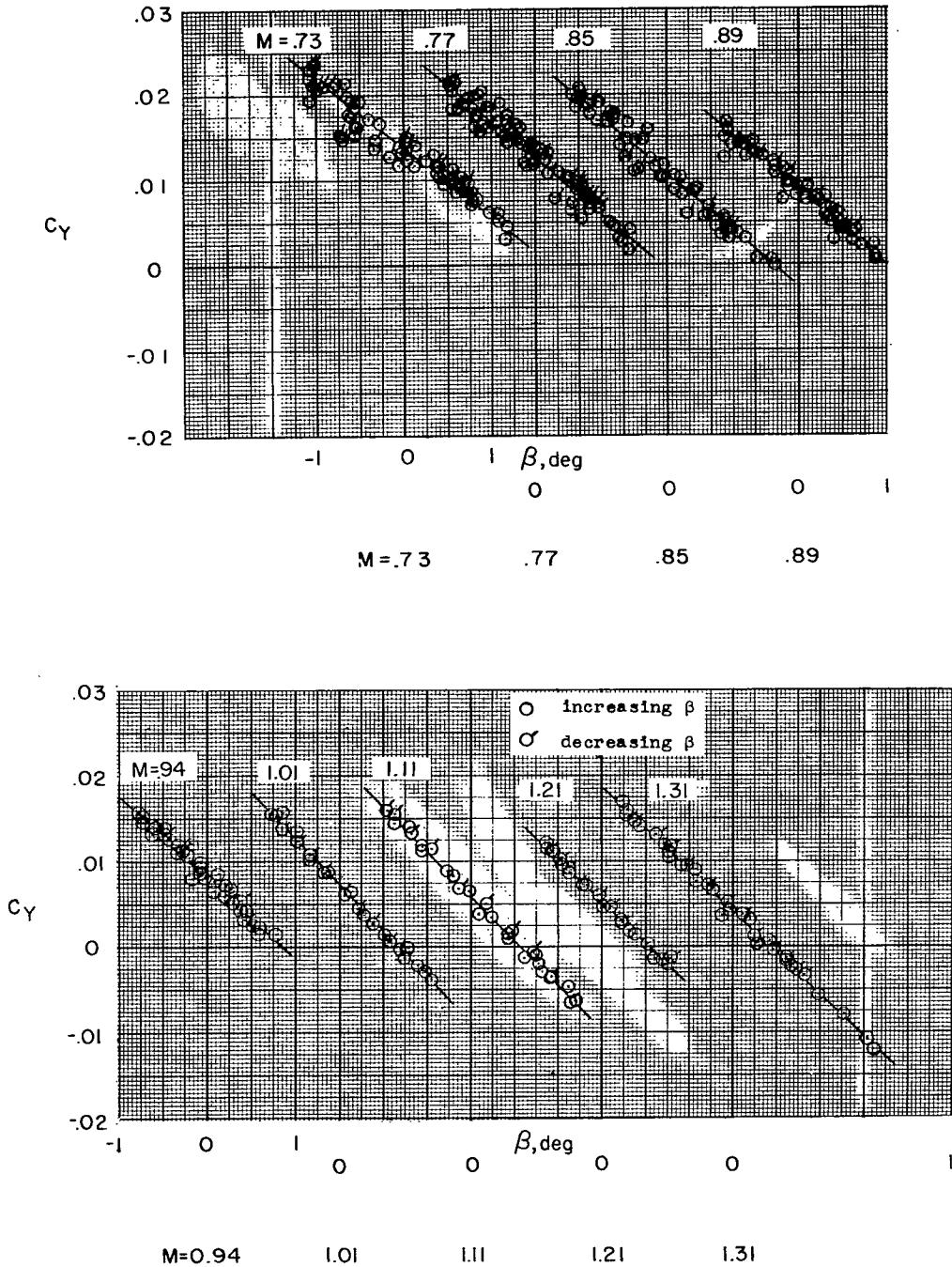
(a) Model 1.   High-wing model.

Figure 15.- Lateral-force coefficients.
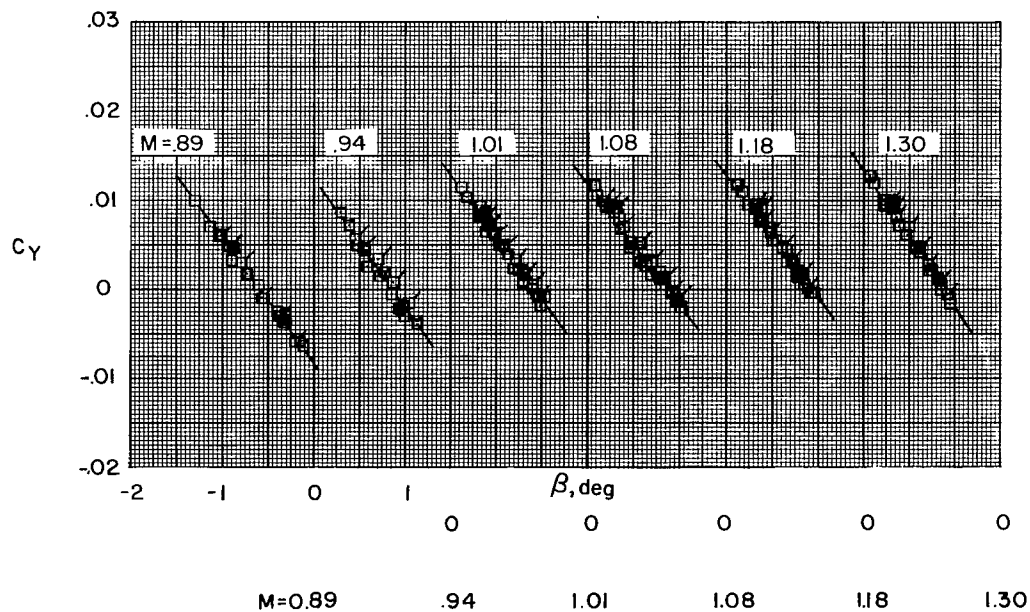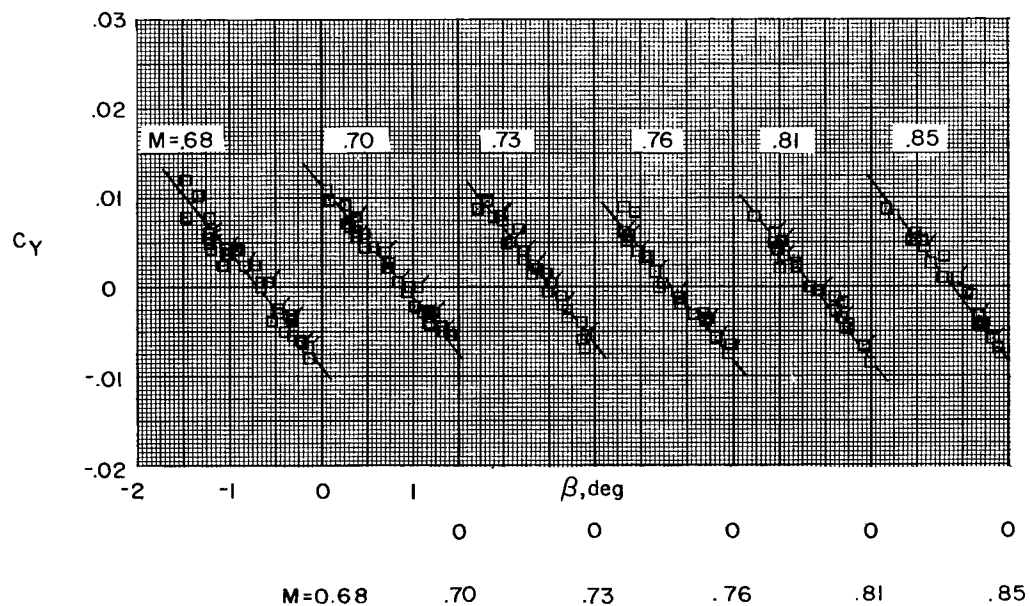
(b) Model 2. Low-wing model.

Figure 15.- Continued.
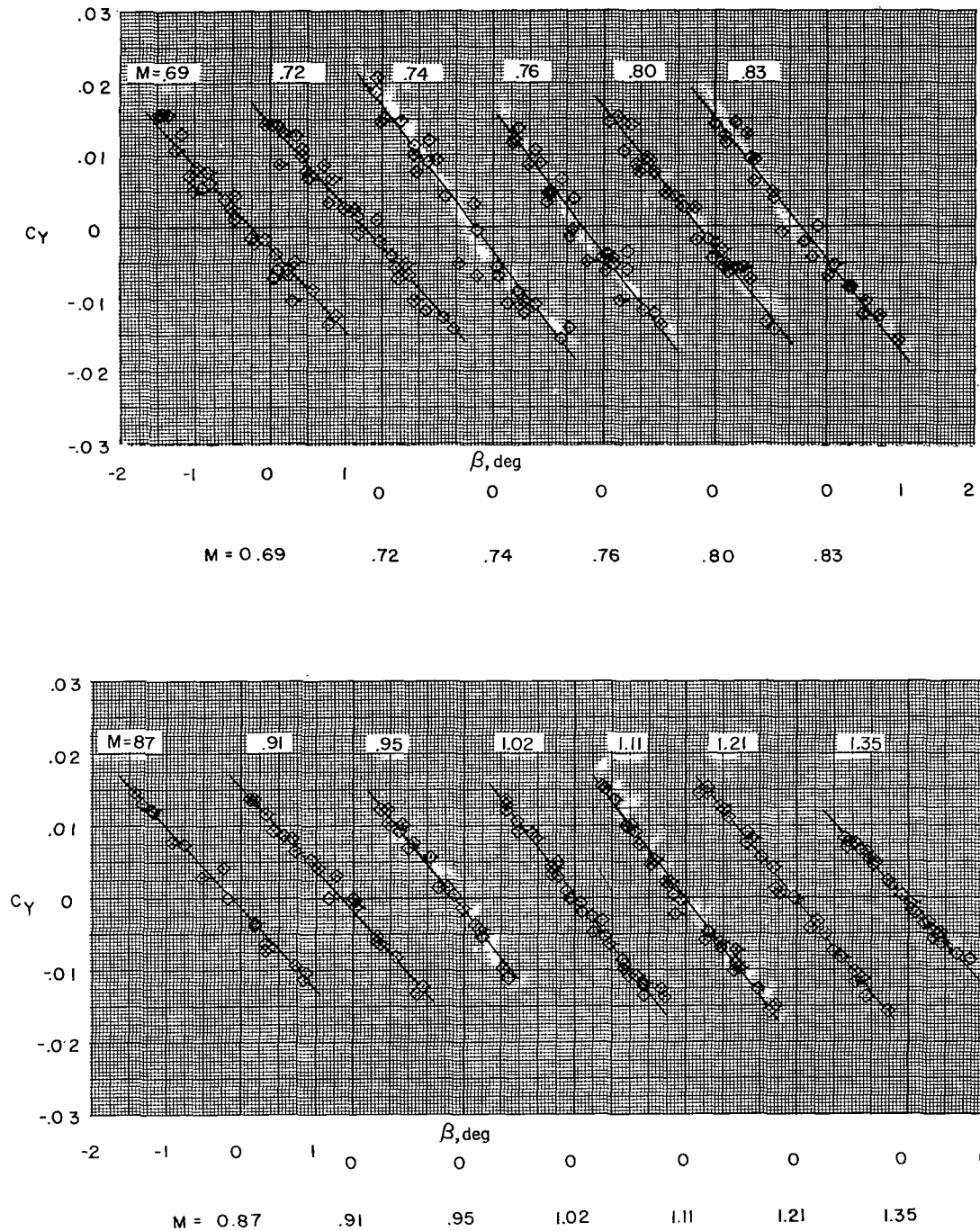
(c) Model 3. High-wing model, 10° cathedral.

Figure 15.- Concluded.
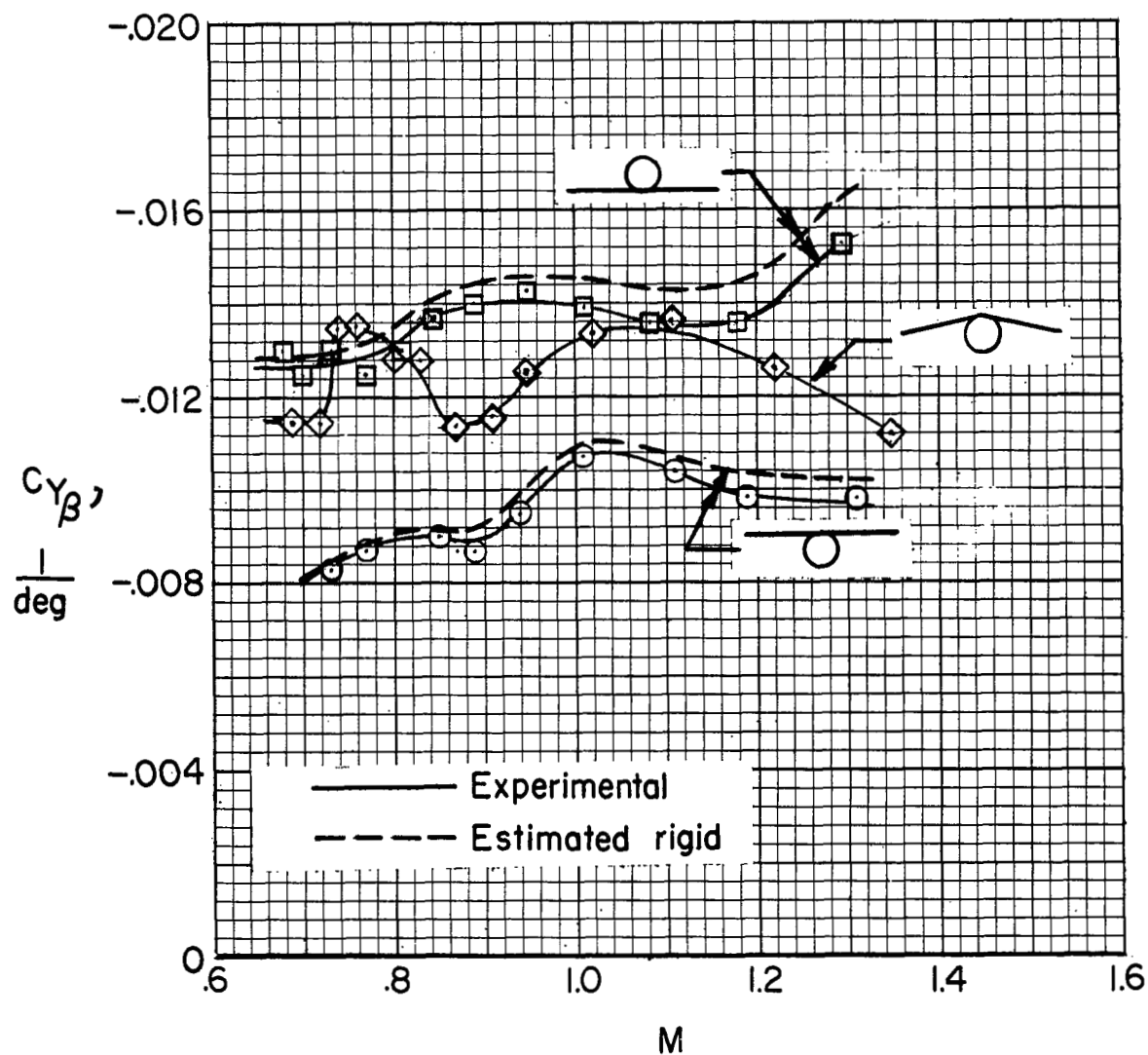
Figure 16.- Static lateral-force derivative.
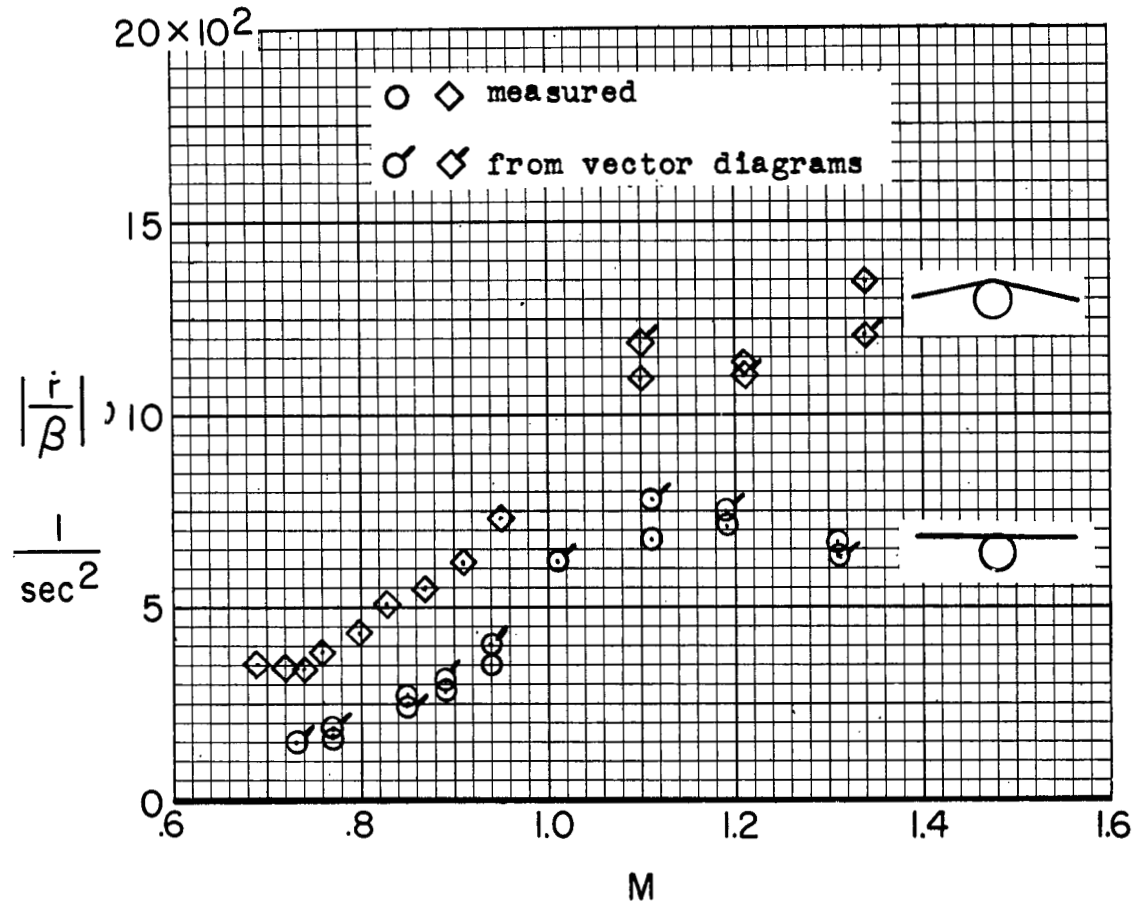
Figure 17.- Yawing acceleration amplitude.
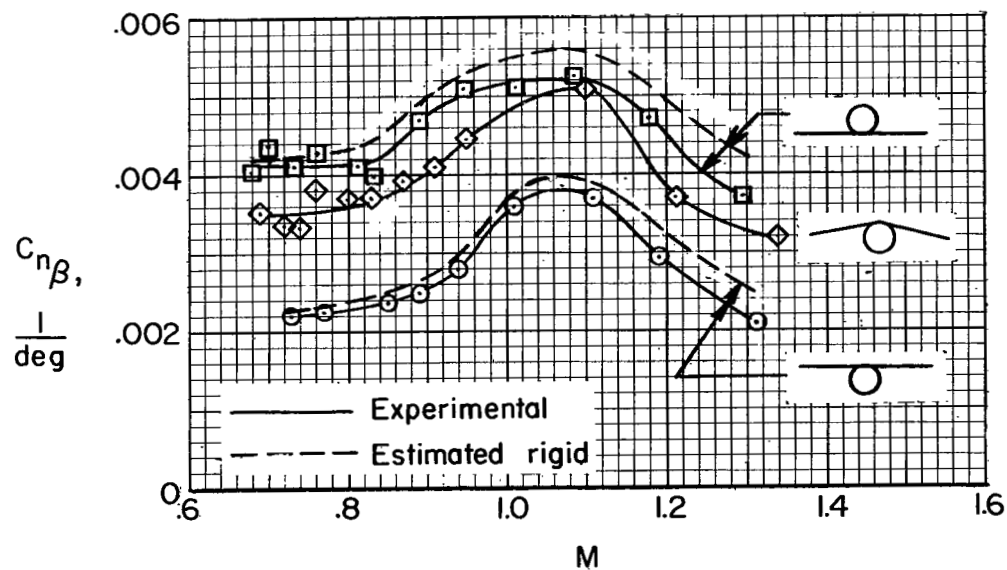
Figure 18.- Static directional stability derivative.
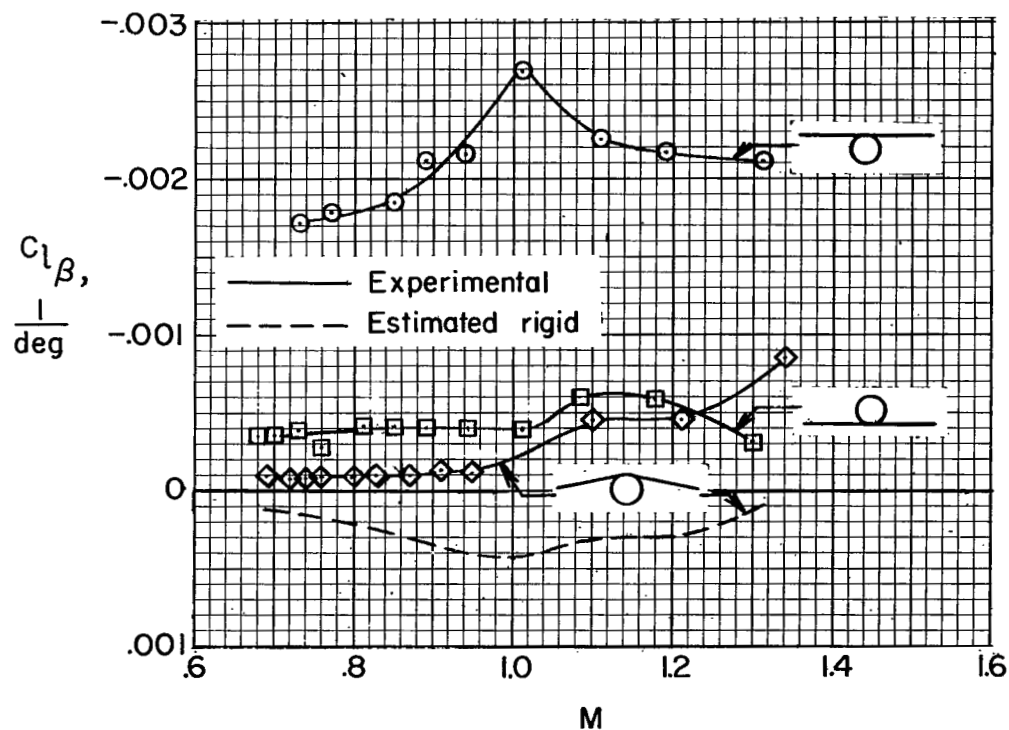
Figure 19.- Effective dihedral derivative.
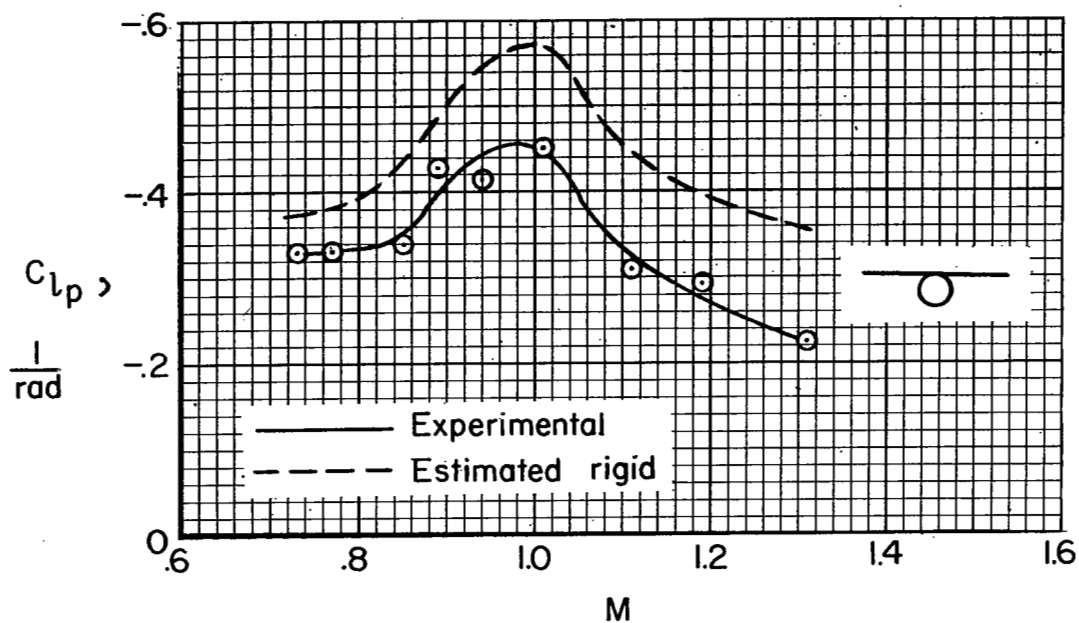
Figure 20.- Damping-in-roll derivative.
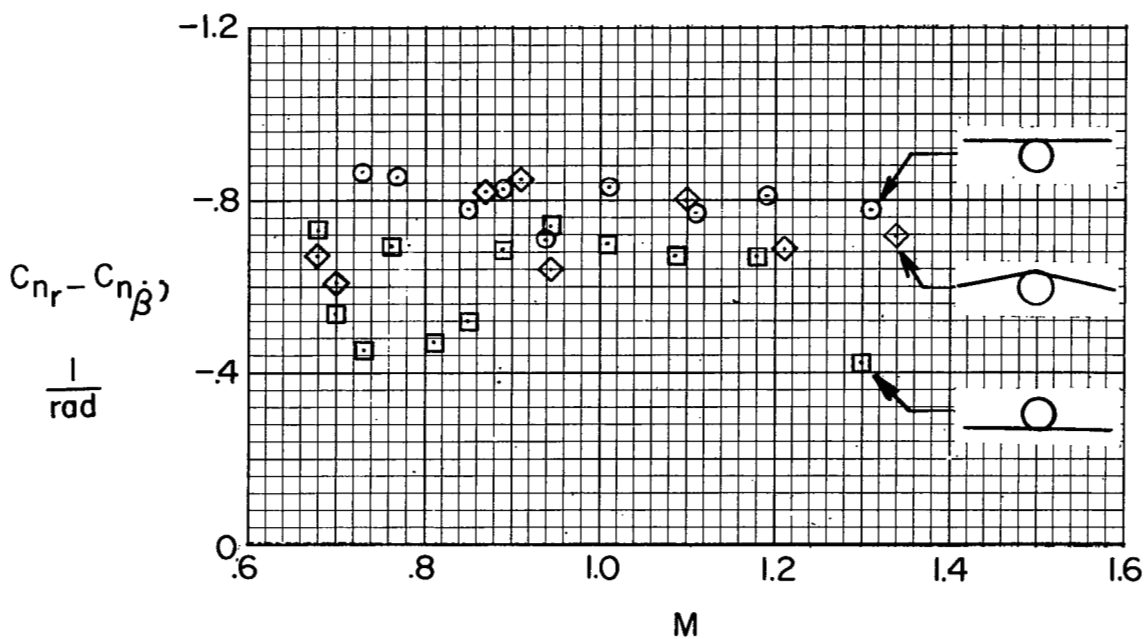
Figure 21.- Damping-in-yaw derivative.
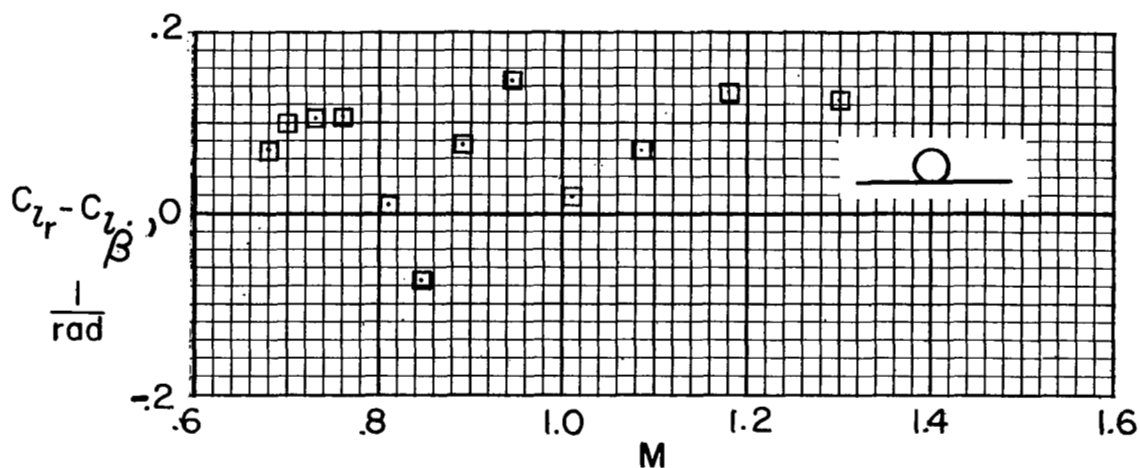
(a) Low-wing model.
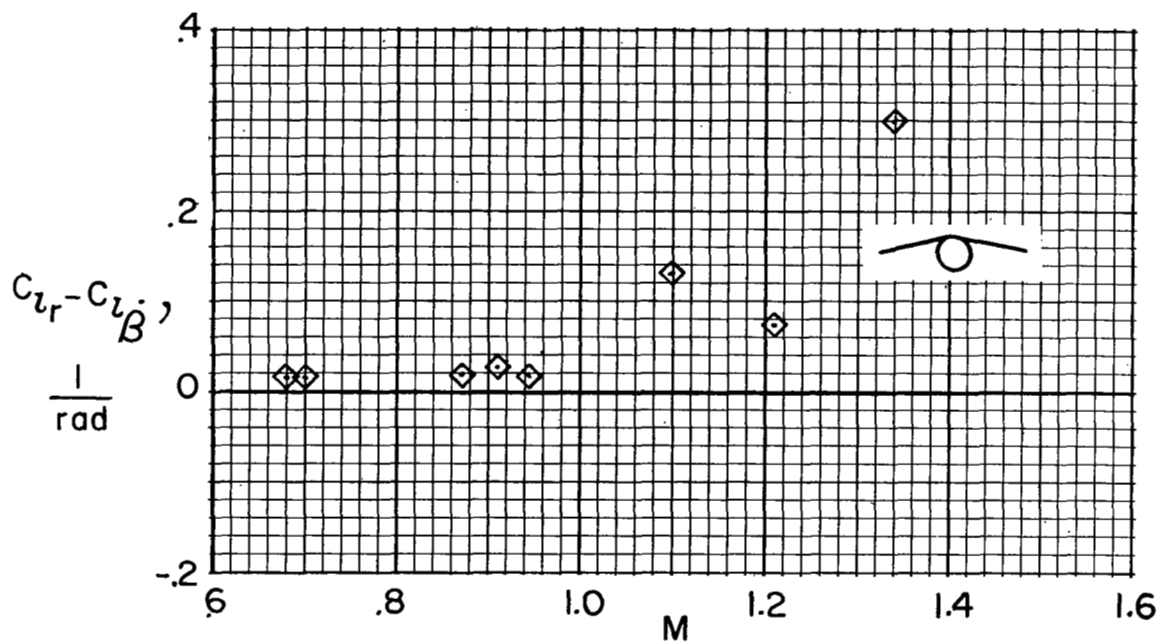
(b) High-wing model, 10° cathedral.

Figure 22.- Lateral stability derivative $C_{l_r} - C_{l_{\dot{\beta}}}$.
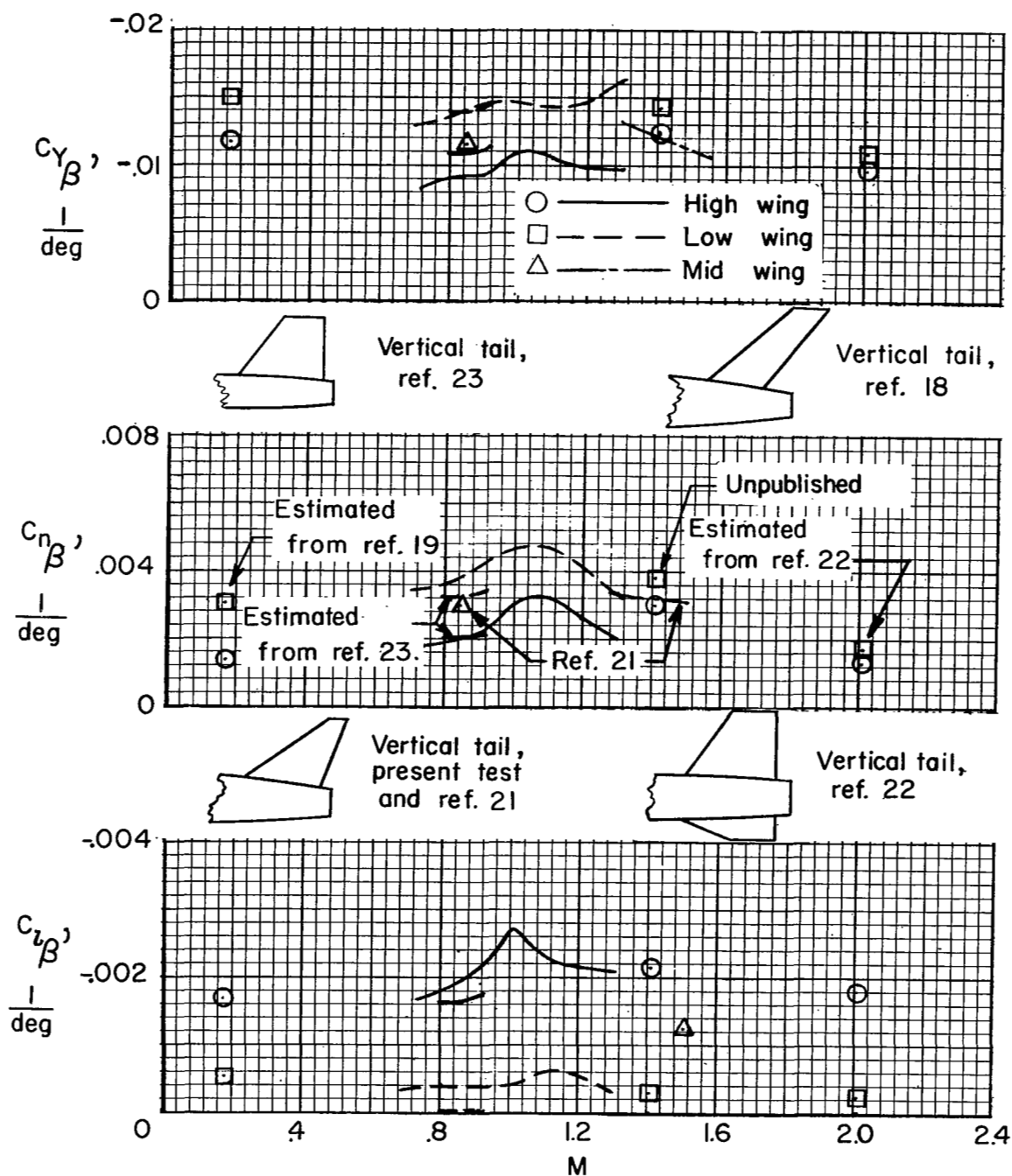
Figure 23.- Comparison of rocket-propelled model and wind-tunnel data
on effects of wing height.
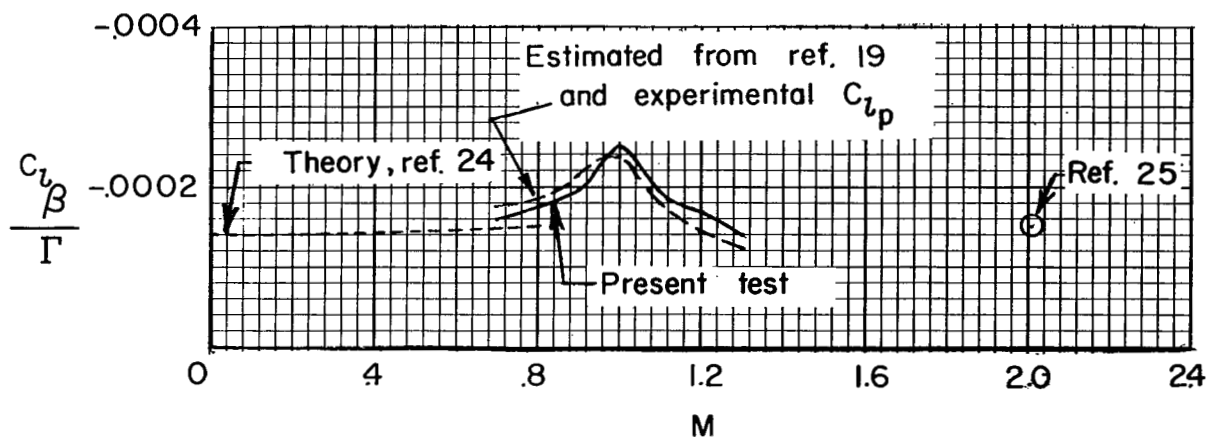
Figure 24.- Effect of geometric dihedral on the effective dihedral derivative C_{l_β}.
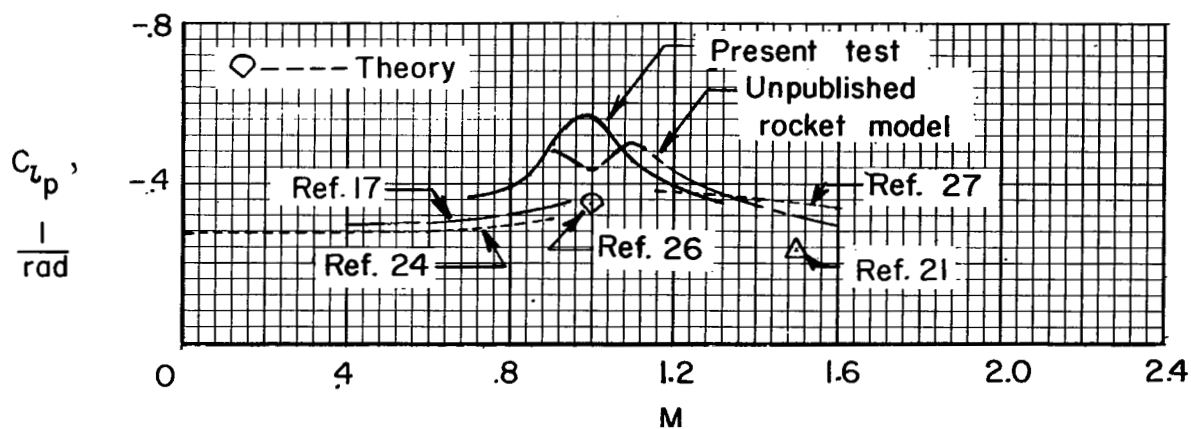
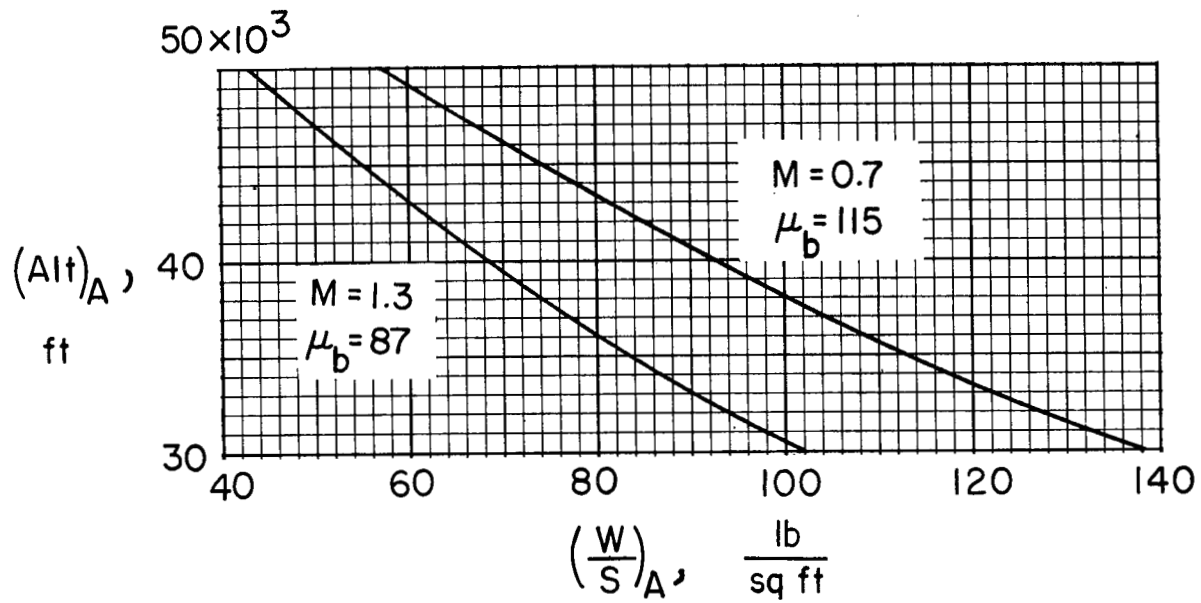Figure 25.- Comparison of rocket-propelled model, wind-tunnel, and theoretical damping in roll.

Figure 26.- Airplane flight conditions simulated by models assuming
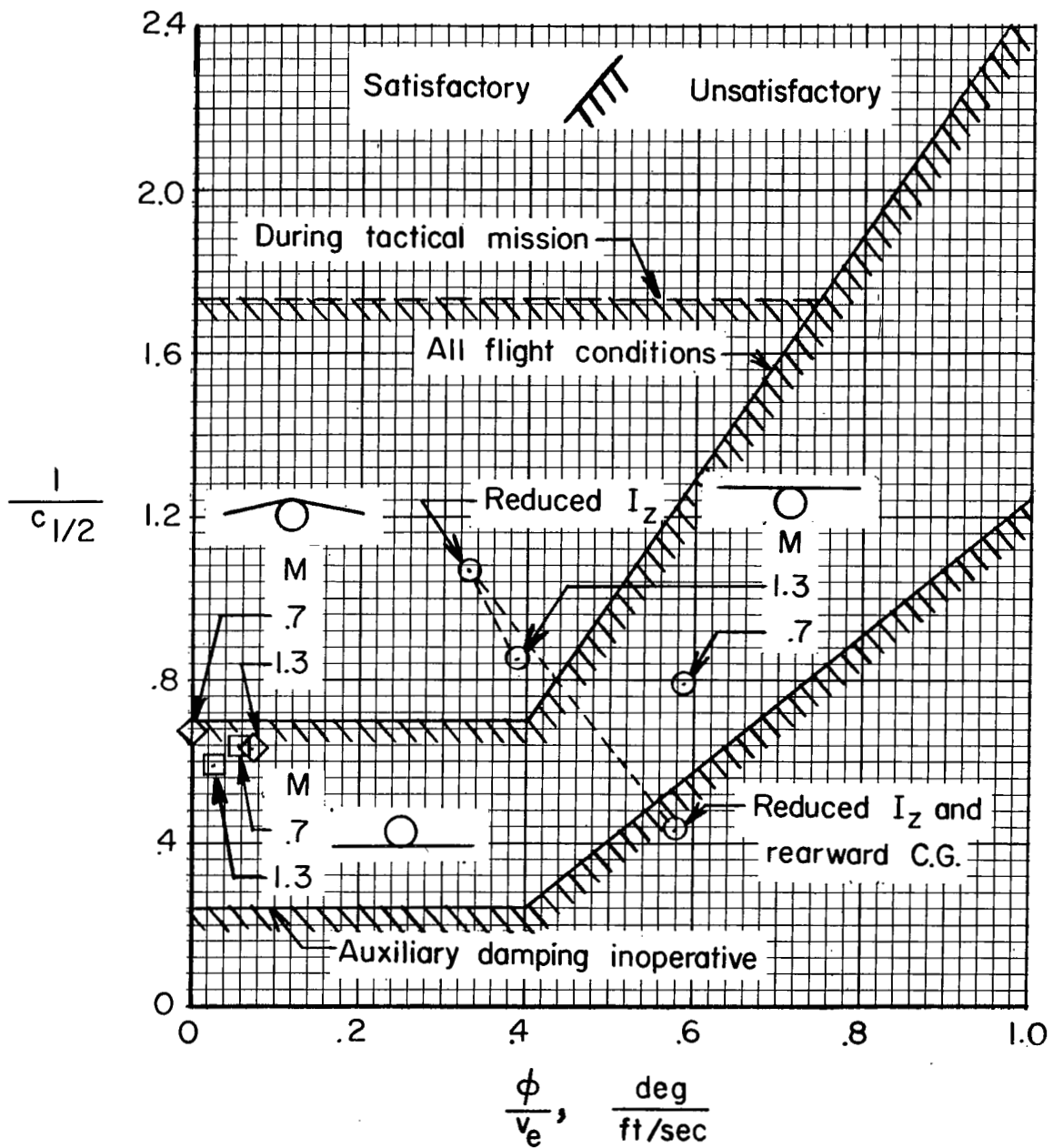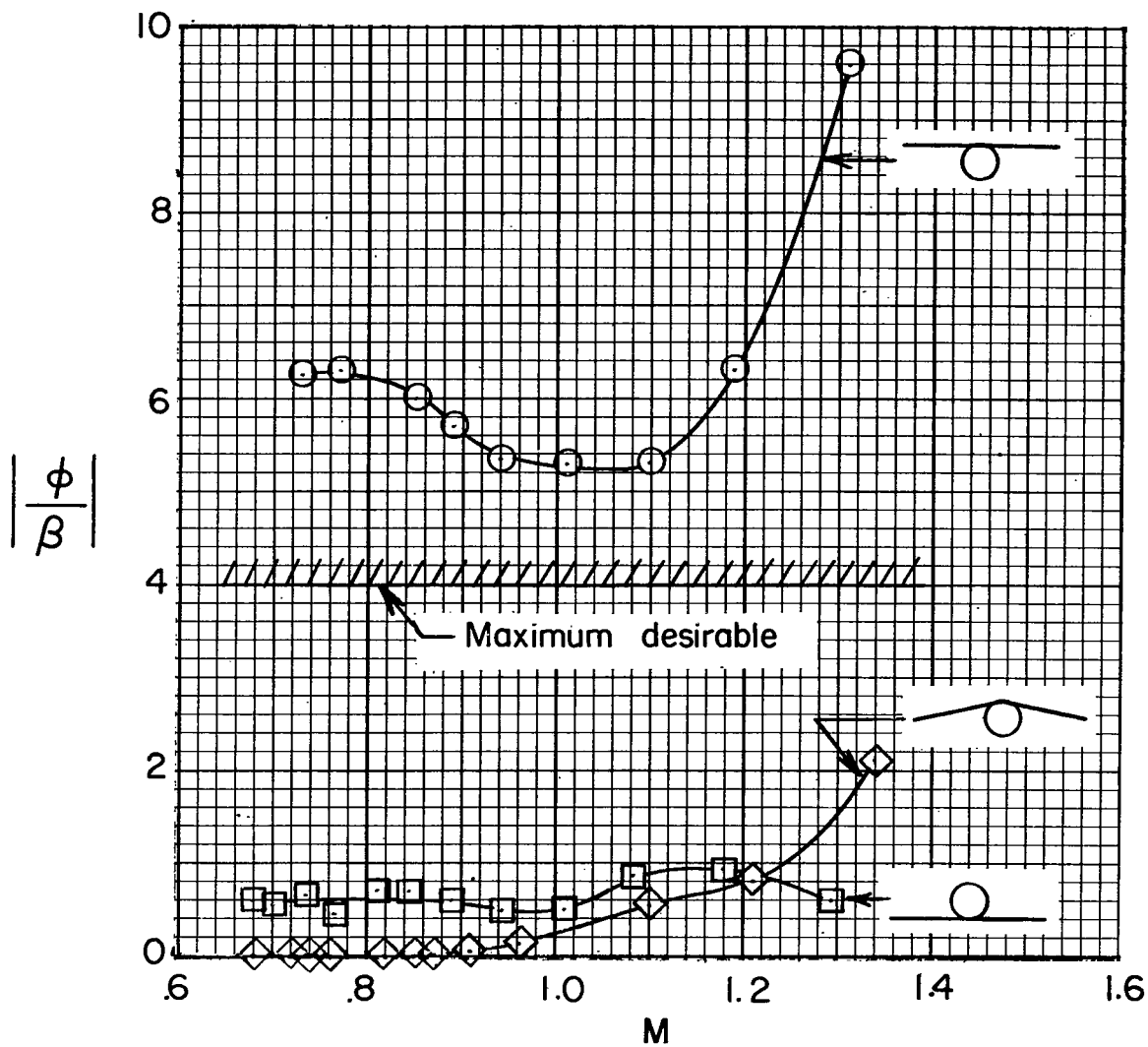10:1 scale factor and same relative density.

Figure 27.- Lateral-oscillation damping requirement.

Figure 28.- Roll-to-sideslip ratios.